UC Santa Cruz

UC Santa Cruz Electronic Theses and Dissertations

Title

Reconstructing the Development of Long-range Parallel Processing Sensory Circuits

Permalink

https://escholarship.org/uc/item/3xm0s4cn

ISBN

9798293871971

Author

Jacobs, Matthew William

Publication Date

2025-08-22

Copyright Information

This work is made available under the terms of a Creative Commons Attribution License, available at https://creativecommons.org/licenses/by/4.0/

Peer reviewed|Thesis/dissertation

eScholarship.org Powered by the California Digital Library
University of California

UNIVERSITY OF CALIFORNIA
SANTA CRUZ

RECONSTRUCTING THE DEVELOPMENT OF LONG-RANGE PARALLEL PROCESSING SENSORY CIRCUITS

A dissertation submitted in satisfaction of the
requirements for the degree of

DOCTOR OF PHILOSOPHY

in

MOLECULAR, CELL, AND DEVELOPMENTAL BIOLOGY

by

Matthew William Jacobs

September 2025

The Dissertation of Matthew William Jacobs is approved:

_____

Professor Euiseok Kim, Chair

_____

Professor Bin Chen

_____

Professor David Feldheim

_____

Peter Biehl

Vice Provost and Dean of Graduate Studies

Copyright © by

Matthew William Jacobs

2025

Table of Contents

ABSTRACT

RECONSTRUCTING DEVELOPMENT OF LONG-RANGE PARALLEL PROCESSING SENSORY CIRCUITS

Matthew William Jacobs

Cortico-cortical projection neurons (CCPNs) connect cortical areas to facilitate distributed computation, sensory processing, motor actions, and complex behavior. In the adult mammalian cortex, CCPNs are organized into circuits that exhibit stereotyped long-range, target-specific, and often reciprocal projections to higher visual areas (HVAs), yet the developmental principles that specify these projection patterns remain poorly defined. Two different mechanisms have been proposed to explain how target specificity arises. In one model, specificity emerges from early inter-regional exuberant outgrowth followed by pruning, while the second proposes that specificity is derived through initially directed axonal targeting. To distinguish between these models, I determined the postnatal trajectory of CCPN axons that project from primary visual cortex (V1) to eleven HVAs in mice during development using rapid and complementary retrograde, anterograde, and single-cell tracing methods. These complementary approaches revealed that V1 neurons overwhelmingly favor single-target projections across development, with minimal evidence for dual

projections or transient exuberance. V1→HVA connectivity develops through a spatially biased temporal sequence of axon outgrowth, where neurons targeting medial HVAs extend axons earlier than those targeting lateral areas, followed by modest, target-specific pruning. Both MAPseq and multiplexed retrograde tracing showed that individual V1 neurons establish and retain distinct projection patterns over time, supporting a model of early specific targeting followed by modest, target-dependent refinement. Additionally, reciprocal feedback projections from HVAs to V1 were refined over time, yielding aligned bidirectional connectivity as expected in adult circuits. These results support a directed guidance model, in which distinct V1 CCPN subtypes establish selective projection patterns early, followed by local, target-specific refinement.

ACKNOWLEDGEMENTS

In my estimation, a good scientist is typically—by nature—a habitual daydreamer, an exhausting pedant, and a naive (and often hapless) engineer. I would like to thank my mentor Euiseok for helping me to embrace each of those innate talents, and for encouraging in me the self-discipline required to bend them into productive scientific pursuits.

I would also like to thank Bin Chen and David Feldheim for being on my thesis committee and for their ongoing support and advice over the years. Bin, your feedback on my early project and oral exam proposals helped to shape my experiments which would become a large part of this dissertation. Dave, I have found your support and advice to be invaluable over the years. I will never forget learning to present project slides in our early joint lab meetings; especially that I should let my title slide do its job and just start talking.

I would like to thank all of the undergraduate research assistants who I have had the privilege of mentoring and who have directly worked to advance my projects over the past six years. In particular, I want to thank Alec Soronow, Jordan Nichols, and Hylen James. Alec, you joined my project right at the beginning and worked tirelessly alongside me as a research assistant, then as a graduate student, then as a co-author. I cannot thank you enough for all of the time, help, and support you have given to this endeavor. Jordan and Hylen, without both of your endless efforts this project would not be what it is today. I am glad to have worked with each of you.

For all their ongoing advice, camaraderie, humor, and daily encouragement I would like to thank Jena Yamada, Brian Mullen, and Tommy Finn. Thank you for all the wonderful little moments and memories stolen from the minutes between the work.

Most importantly, thank you to my family. Daniella, for so many years of support and encouragement through thick and thin, for helping me on a daily basis, for our family, and for our life together. Thank you, I could not and would not have done this without you. Henry and Emmett, thank you both for keeping me young and excited by the little wonders in life. To my parents, thank you for a lifetime of hard work and support spent on my childhood dream of being a scientist. I love you all very much.

To all the rest left unmentioned, who each deserve their own pages of praise, thank you all from the bottom of my heart.

The text of this dissertation includes draft portions of the following manuscript in preparation for submission:

Structured and Target-Specific Development of Cortico-Cortical Connectivity in the Mouse Visual Cortex

Matthew W. Jacobs[1,2], John M. Ratliff[1,2], Alec L.R. Soronow[1], Jordan A. Nichols[1], Hylen T. James[1], Jorin A.G. Eddy[1], Adam M. Murray[1], Euiseok J. Kim[1,3]

[1]Department of Molecular, Cell, and Developmental Biology, University of California, Santa Cruz, CA 95064

[2]Co-first author, [3]Corresponding author

*Corresponding Author: Euiseok J. Kim

Department of Molecular, Cell, and Developmental Biology, University of California, Santa Cruz, 1156 High Street, Santa Cruz, CA 95064, USA

Phone: 831-502-7233
Fax: 831-459-3139
ekim62@ucsc.edu

Acknowledgement for Jacobs et. al., 2025;

We thank Edward Callaway, Bin Chen, Bradley Colquitt, David Feldheim, and Yi Zuo for reading the manuscript and Efrain Hernandez-Alvarez for mouse husbandry and histology. We thank Huiqing Zhan and John Hover at the Cold Spring Harbor Laboratory MAPseq core for their technical support and guidance. We thank John Naughton and members at the Salk Institute GT3 virus core for AAVs and VSV reagents. We acknowledge technical support from Benjamin Abrams, UCSC Life Sciences Microscopy Center, RRID: SCR_021135. Purchase of the Zeiss 880 confocal microscope used in this research was made possible through the National Institutes of Health s10 Grant 1S10OD23528-01. We acknowledge support from the UCSC start-up fund, the Whitehall Foundation, the Hellman Fellows Program, the E.

Matilda Ziegler Foundation for the Blind, BRAIN Initiative at the National Institutes of Health RF1MH132591, the National Institute of Neurological Disorders and Stroke at the National Institutes of Health R01NS128771 (E.J.K.), and the Koret scholar program (A.L.R.S.). Portions of the text in this manuscript were edited solely for clarity and grammar using ChatGPT (GPT-4 Turbo, OpenAI); no content or scientific interpretation was generated by the language model.

Chapter 1: Introduction

In the mammalian cerebral cortex, the transformation of sensory inputs into coherent percepts is mediated by inter-areal connectivity between hierarchically organized cortical regions (Felleman and Van Essen, 1991; Harris et al., 2019; Zeki and Shipp, 1988). The proper development of cortico-cortical connections is essential for neocortical functions such as hierarchical computation, multisensory integration, and the control of complex behavior (Felleman and Van Essen, 1991; Harris, K. D., and Mrsic-Flogel, T.D., 2013). Disruptions to this process are implicated in neurodevelopmental and psychiatric disorders characterized by aberrant inter-areal connectivity, including autism spectrum disorder and schizophrenia (Baker et al., 2014; Haberl et al., 2015). Understanding how these connectivity patterns form is critical to explaining how long-range cortical networks acquire their mature functional architecture.

In mice, cortico-cortical projection neurons (CCPNs) in the primary visual cortex (V1) project to at least ten anatomically and functionally distinct higher visual areas (HVAs), forming precise circuits that support visual information processing (Wang and Burkhalter, 2007; Kim et al., 2020; Glickfeld et al., 2013; Marshall et al., 2011). In the adult brain, CCPNs show clear target specificity: some project to a single HVA as dedicated information channels, while others innervate multiple HVAs in a non-random, structured manner, functioning as broadcasting channels (Han et al., 2018). Furthermore, reciprocal feedback from HVAs often targets the same

subpopulations of V1 neurons that project to them, forming “like-to-like” connectivity motifs (Kim et al., 2020; Young et al., 2021). However, the developmental basis of this specificity remains poorly understood.

Two main developmental mechanisms have been proposed to explain how CCPNs acquire long-range target specificity (Kast et al., 2019; Innocenti et al., 2005). The exuberant growth and pruning model suggests that immature neurons initially send axons to multiple targets, followed by activity-dependent pruning of incorrect or redundant axonal branches, resulting in refined adult patterns (Luo and O’Leary, 2005; Innocenti et al., 1977; Katz and Shatz, 1996; Sanes and Lichtman, 1999; Callaway and Katz, 1990). In contrast, the directed guidance model posits that target specificity is largely established early in development, driven by intrinsic genetic programs and molecular cues that guide target-directed axonal growth (Klingler et al., 2021; Molyneaux et al., 2007; Barone et al., 1996). These two models are not mutually exclusive, but they make distinct predictions about when and how CCPNs select their targets, and whether projection motifs are refined from a broad, undifferentiated state or are specified from the outset. Distinguishing between these models in the context of multi-area cortico-cortical circuit development has been challenging, partly due to technical limitations in tracing the full axonal output of individual neurons across development with spatial and temporal resolution.

To address these limitations and distinguish between exuberant pruning and directed axon guidance as mechanisms of projection specificity, I systematically

traced the developmental trajectories of feedforward and feedback connectivity between V1 and HVAs. I accomplished this using a combination of chemical and viral anatomical tracing strategies—including cholera toxin subunit B (CTB), vesicular stomatitis virus (VSV), AAV-retrograde vectors, and barcoded Sindbis virus—to capture the spatial, temporal, and single-cell specificity of V1→HVA circuit formation.

Using a combination of rapid dual and sequential retrograde labeling, bulk anterograde tracing, and quantitative histology, I found that CCPNs targeting medial and lateral HVAs emerge in a biased temporal sequence, with axons to medial areas appearing days earlier than those to lateral ones. Bulk anterograde tracing confirmed that medial projections mature gradually, whereas lateral projections exhibit a transient phase of exuberant overgrowth followed by rapid pruning. Extended survival retrograde experiments ruled out large-scale cell death as a mechanism for circuit refinement, implicating axon pruning within defined target regions instead. Additionally, feedback projections from HVAs to V1 displayed relatively little spatial or temporal heterogeneity, and progressively aligned with feedforward outputs to form reciprocal “like-to-like” motifs.

To capture these dynamics at single-cell resolution, I used the MAPseq (Multiplexed Analysis of Projections by Sequencing) platform (Kebschull et al., 2016) to label and quantify the axonal projection motifs of thousands of individual V1 CCPNs across developmental timepoints. MAPseq revealed that the number of

target areas innervated per neuron, the complexity of their projection motifs, and the frequency of dedicated versus broadcasting profiles were largely consistent from early postnatal stages through adulthood.

Together, these results support a directed guidance model in which target specificity is established early, followed by area- and time-specific refinement through pruning—not large-scale axonal reorganization. Rather than initially wiring to many areas and then collapsing to a final motif, V1 CCPNs selectively innervate their mature targets through a structured and stereotyped developmental program.

Chapter 2: Results

Axonal targeting from V1 to AL and PM occurs via directed projection during development

It is known that adult V1 CCPNs communicate with HVAs using at least two distinct modes: predominantly dedicated projections to a single target area, or less frequent broadcasting projections to multiple areas following specific patterns (Kim et al., 2020; Han et al., 2018) (Figure 1a). As an example of the dedicated mode, two largely non-overlapping V1 CCPN populations project to either AL or PM (V1→AL or V1→PM CCPNs, respectively), without sharing axon collaterals across these targets.

To distinguish between two competing models of long-range cortical circuit formation—early exuberant axonal outgrowth followed by pruning versus directed, target-specific projection—I examined the developmental trajectory of V1→AL and V1→PM connectivity in juvenile mice. I accomplished this by injecting Alexa fluorophore-conjugated cholera toxin subunit B (CTB) into AL and PM at postnatal days P3, P6, P12, and P60+. Tracing experiments run prior to P3 revealed little cortico-cortical activity, so I chose P3 as my starting earliest developmental stage. P12 was chosen to correspond with the eye-opening phase of murine development. P6 (and P20 in later experiments) was chosen to bridge developmental gaps between these known developmentally important points. Then, I quantified the numbers and proportions of V1→AL and V1→PM CCPNs 3–6 days after injection, including the

degree of dual labeling observed in each group (Figure 1a-b). If V1 CCPNs initially extend axons exuberantly to multiple areas, a higher proportion of neurons co-labeled for both AL and PM projections would be expected during early developmental stages compared to adulthood (Model 1, Figure 1b'). In contrast, if CCPNs form specific projections early on, the proportion of dual-labeled cells would remain low (Model 2, Figure 1b'). AL and PM injections were targeted in young animals using a combination of surface vascular landmarks. To ensure the specific targeting of the targeted HVA at early postnatal stages, I screened each labeled brain by examining whole-mount and coronal sections of the cortex and thalamus (Figure 1c-d). Injections into AL and PM were considered accurate only when post hoc examination of the injection signal was confined within HVA borders, and there was no spillover of locally labeled cells into adjacent regions. To achieve this, I screened injections further by confirming the absence of CTB-labeled neurons in the dorsal lateral geniculate nucleus (dLGN), which projects to V1 (Figure 1e). Additionally, CTB signal was commonly observed in more posterior and lateral thalamic regions, such as the lateral posterior nucleus (LP) and posterior (PO), which are known to project to HVAs and may reflect accurate labeling of higher-order visual thalamocortical loops (Wang and Burkhalter, 2007). Further, in cases where signals were found in the medial geniculate dorsal subdivision (MGD) (reflecting some quantity of auditory cortex injection contamination (Hackett, T. A. (2011)) animals were excluded for injection accuracy (Figure 1e).

Across all developmental stages examined, the fraction of dual-labeled V1→AL+PM neurons was low (P3→P6: 1.4 ± 0.3%, n=3; P6→P9: 2.3 ± 0.5%, n=4; P12→P18: 1.3 ± 0.2%, n=3; P60+→P65+: 2.3 ± 0.7%, n=3; mean ± SEM)(See methods for clarification on age notation nomenclature used in this document). These data support the direct guidance Model , indicating that V1→AL and V1→PM projections are established as early as P9 (AL) and P6 (PM), and remain until adulthood. This is consistent with a prior study in adult mice which hypothesized that target-specific axon guidance, rather than exuberant multi-target innervation followed by pruning, is the mechanism used by V1 to project to HVAs (Klingler et al., 2021).

I next asked whether laminar distribution of V1→AL and V1→PM neurons changes over time, or whether layer-specific targeting is also established early. To do this, I quantified the laminar position of V1→AL, V1→PM, and V1→AL+PM CCPNs across the same developmental stages. At P3→P6, V1 layer 5 (L5) neurons predominantly projected to PM, with minimal labeling of V1→AL neurons in any layer. By P6→P9, deep-layer V1→PM projections persisted, and a subset of L5 neurons began projecting to AL. At P12→P18, V1→PM neurons emerged in L2/3 upper, while new V1→AL neurons appeared in L2/3 in addition to L5 V1→AL CCPNs. In adults (P60+→P65+), cell distributions were found to match previously reported findings for mature animals: V1→PM projections were concentrated in L5 and L2/3 upper layers, whereas V1→AL projections localized primarily to L2/3 lower (Kim et al., 2020; Han and Bonin, 2024; Cheng et al., 2022) (Figure 1h–i).

These data support a spatiotemporally defined projection program, where layer identity and target specificity co-emerge during early postnatal development.

Finally, to test whether dedicated V1→AL and V1→PM populations remain distinct over time or undergo target switching through pruning and redirection, I used a sequential dual-retrograde labeling strategy. To test this, I performed sequential injections of long-term labeling retrograde tracers: AAVretro-H2B-eGFP into PM at P3 and AAVretro-H2B-mCherry into AL at P35, harvesting at P45 (Figure 1k). This approach was chosen over CTB, which exhibits relatively weak signal intensity after prolonged incubation, particularly when injection volumes are small. I quantified the proportion of double-labeled V1 neurons out of the H2B-eGFP+ (early PM-projecting) population (Figure 1l). If many neurons redirected axons from PM to AL, I would expect higher double-labeling in the sequential group (model 1). However, the proportion of colabeled neurons in the experimental group was not significantly different from that in control animals injected in both areas at P35 and harvested at P45 (Figure 1m). Together with the low dual-labeling observed in CTB experiments, these findings show that V1→AL and V1→PM populations form early, remain largely distinct throughout development, and do not undergo large-scale projection switching.

Global axon output from V1 CCPNs follows a spatiotemporally heterogeneous developmental trajectory

While retrograde tracing offers precise information about neurons projecting to specific targets, it is inherently limited by the number of injection sites and

distinguishable fluorophores. To overcome these limitations and expand on the target specific developmental dynamics revealed through the targeted retrograde tracing experiments, I used a glycoprotein-deleted negative-strand RNA Vesicular Stomatitis Virus (VSV) expressing tdTomato (VSVdG-tdTomato) pseudotyped with VSV glycoprotein (VSVG) to efficiently and rapidly label axons within four days of injection (Figure 3a). Harvested brains were appropriately prepared and imaged for analysis using Bell Jar (see methods), an image processing software designed for semi-automated feature detection and quantification across brain regions (Soronow et al., 2025) (Figure 2b). In this study, I applied a new module within the Bell Jar framework—a supervised machine learning classifier termed RSAT (Region-Specific Axon Tracer)—to improve automated segmentation of axons across heterogeneous signal densities. Using this classifier within the established Bell Jar pipeline, axon projection data were segmented as binary pixel counts and aligned to the Allen Mouse Brain Common Coordinate Framework Reference Atlas (CCFv3) for target areas including RSPv, RSPd, RSPagl, PM (VISpm in CCFv3), AM (VISam), A (VISa), RL (VISrl), AL (VISal), LM (VISl), LI (VISli), and POR (VISpor). To assign cortical regions across developmental stages, I used Bell Jar's automated alignment to register each sample to the adult Allen CCFv3 atlas. While proportional scaling can be used to roughly map the developing brain, brain growth is known to be nonlinear and regionally heterogeneous (Kronman et al., 2024; Wang et al., 2020; Li et al., 2025; Liwang et al., 2023). To account for these developmental differences, I manually reviewed and adjusted all region boundaries for my areas of interest using

classical cytoarchitectural landmarks based on the Paxinos and Franklin atlas (Figure 14). This ensured that my atlas alignments were accurate in a regionally specific way. To evaluate RSAT's performance as a classifier, I compared its output against manual annotations by two expert raters across both sparsely and densely labeled datasets. Performance was quantified using standard classification metrics: precision, which measures the proportion of predicted axon pixels that are true axons (true positives / [true positives + false positives]), and recall, which reflects the proportion of all actual axon pixels correctly identified by the algorithm (true positives / [true positives + false negatives]). RSAT's precision and recall scores closely matched human-human interrater values (Figure 2a–e), confirming its reliability across labeling densities. I also quantified the number of starter neurons (tdTomato+ soma at injection sites) to normalize axon output as axon pixels per starter neuron (Figure 4c).

Using this rapid anterograde tracing approach, I next determined the developmental trajectories of V1 CCPN axonal projections to eleven different cortical targets, including HVAs. In the earliest age group (P3→P7), axons preferentially infiltrated medial cortical areas such as RSPv, RSPd, RSPagl, and PM. In contrast, lateral areas including AL, LM, LI, and POR showed relatively sparse axon labeling (Figure 3c), consistent with the CTB data (Figure 1h-i). In the following P12→P16 age group, axonal projections expanded broadly, with increased labeling observed across many target areas (Figure 3f). During this expansion phase, the proportional share of axon labeling in medial areas decreased from 86% to 28%, while lateral areas increased from 14% to 72% (Figure 3e, top). HVAs POR and A, showed only

modest increases over the same time period, indicating that this broad expansion of axons is spatially restricted (Figure 2d). By P20→P24, axons were distributed broadly, but specific reductions were observed in lateral areas RL, AL, LM, LI, and POR (Figure 3f). These lateral areas exhibited large increases in axon infiltration during the gap between the experiments at P3→P7 and P12→P16, followed by pruning to levels comparable to adult brains. In contrast, medial regions, including A, AM, PM, and all RSP subregions, followed a more gradual pruning trajectory with mature axon projection patterns not fully established until after P24 and reaching adult-like states by P60+→P64+ (Figure 3c–f).

In order to comprehensively characterize the laminar distributions of detectable axons in HVA targets, I generated axon depth profiles from all Bell Jar-processed images of VSV traced axons(Figure 5). For each animal, axon signals were collapsed across coronal section images to create 1×100 numeric arrays of axon+ pixel count values from the pia mater to the white matter in arbitrary space. Clustering of these depth profiles (n=139, target areas) using Pearson's correlation and Ward's method identified two major projection types: Cluster 1 (deep-layer, DL; n=50) and Cluster 2 (multi-layer, ML; n=89), along with a non-projecting (NP) group where axons were not detected (n=15) (Figure 5b-c). Tracking these clusters across development revealed that medial HVAs were dominated by DL-type projections at P3→P7, while lateral HVAs showed mostly NP profiles, indicating little to no input. By P12→P16, ML projections became prominent in lateral HVAs (Figure 1f). These

results suggest that laminar targeting of V1 CCPNs follows distinct, area-specific developmental trajectories.

My findings show that the V1→PM before V1→AL developmental dynamics revealed through targeted retrograde tracing (Figure 1) generalizes to a broader medial-before-lateral scheme across additional HVAs. Furthermore, V1 CCPNs undergo regionally and temporally distinct phases of exuberance and pruning. Rather than following a uniform developmental timeline, axonal refinement proceeds according to a spatiotemporally organized plan: projections to medial HVAs emerge earlier but mature more slowly, while those to lateral HVAs arise later and refine more rapidly.

Together, these results reveal a novel, target-dependent developmental program in which the timing and laminar specificity of axon growth and pruning differ systematically across higher visual areas. While prior studies have described laminar or target specificity in the mature cortex, my data are the first to show that individual cortical projection neurons follow these area-specific developmental trajectories during the postnatal period, with distinct time courses of axon infiltration expansion and refinement depending on their target. This temporally and spatially structured developmental logic suggests that target identity is encoded early and guides not only initial targeting but also the pace of circuit maturation, providing new insight into the mechanisms underlying the emergence of functional cortical networks.

Axonal pruning, rather than apoptosis, underlies the reduction of laterally projecting V1 axons during the second postnatal week

To determine whether the developmental reduction in axon coverage, particularly in lateral HVAs, is the product of axonal pruning (Figure 6a, top right) or apoptosis (Figure 6a, bottom right) of source cells in V1, I compared the density of labeled neurons in V1 after short and long viral incubation periods following retrograde labeling of axons exuberantly innervating lateral higher visual areas during the P12→P16 period (Figure 6b). If V1 CCPNs projecting to lateral areas such as LM undergo apoptosis (Cai et al., 2024), a longer incubation (20 days) after injection at P10 would yield fewer labeled V1→LM neurons than a shorter incubation (5 days). In contrast, if pruning occurs without cell loss, the number of labeled neurons would remain stable despite reduced axonal density. To test this, I injected AAVretro-H2B-eGFP into LM at P10 and harvested brains after 5 or 20 days (Figure 6b), capturing neurons during peak projection and post-refinement periods (P12→P24), when the most prominent reduction in lateral axon coverage is observed.

I quantified retrogradely labeled V1→LM CCPNs across every other coronal section through the entire V1 (Figure 6b bottom), measured the area of tissue containing labeled cells, and calculated cell density (cells/area) for each section (Figure 6c). These values were normalized to the number of labeled cells at the injection site to control for variation in injection efficiency, as well as a growth factor to account for the increase in brain size between P15 and P30 (see methods). This reveals that there is no significant difference in the number of retrogradely labeled

V1→LM CCPNs between the 5-day and 20-day incubation groups ($p = 0.5618$, Student's t test, Figure 8d and 15d), supporting axon pruning as the mechanism underlying the observed reduction in axon coverage in lateral HVAs between P16 and P24. As a control experiment, a similar analysis in adult P60+ animals also showed no significant difference ($p = 0.8023$, Student's t test), suggesting that neither viral toxicity nor expression levels affected the results (Figure 6d). Analysis of the laminar distribution of retrogradely labeled V1→LM CCPNs revealed no differences between short and long incubation groups within either pups or adults (Figure 6e). However, developmental versus adult comparisons showed a clear shift from predominantly deep layer labeling in pups to increased upper layer representation in adults (Figure 8e), consistent with the CTB tracing results (Figure 1h–i). Taken together, these findings indicate that developmental reduction in lateral axon projections results from selective axon pruning rather than neuron loss (Figure 4a, top right).

Developmental trajectories of feedback inputs to V1 and emergence of reciprocal cortico-cortical connectivity

To complement the VSVdG-mediated axon output tracing of V1 to 11 cortical areas (Figure 3), I examined the developmental trajectory of feedback input from the same areas to V1 using retrograde labeling with AAVretro-H2B-eGFP (Figure 8a). Injections of AAVretro-H2B-eGFP into V1 were performed across the same postnatal time windows as the bulk anterograde tracing experiments (P3→P7, P12→P16, P20→P24, and P60+→P64+), after which coronal sections (50 μm) were imaged and registered to the Allen CCFv3 atlas using Bell Jar. Retrogradely labeled H2B-eGFP+

feedback input neurons were manually quantified across all eleven higher cortical areas (Figure 8b-c and 15), and counts were normalized to the number of labeled starter neurons at the V1 injection site to account for variability in infection and tracing efficiency.

Although mature interareal connectivity is often reciprocal, feedforward and feedback projections between V1 and HVAs develop along distinct, uncoordinated trajectories. Based on normalized feedback neuron counts and their proportions across cortical areas, I did not observe statistically significant changes in the overall magnitude or distribution of higher-order cortical inputs to V1 during development, although a weak decreasing trend was evident (Figure 8c, f). Spatially, the medial-lateral and anterior-posterior distribution of feedback input neurons remained largely stable across developmental stages. However, some region-specific differences emerged over time, including a tendency for reduced input from medial areas (RL, AL, LM, LI, POR) relative to lateral areas (A, AM, PM, RSPagl, RSPd, RSPv), as well as from posterior regions (AM, PM, RSPagl, RSPd, RSPv, LM, LI, POR) relative to anterior regions (A, RL, AL) (Figure 8d–e). Notably, feedback input from RSPd and RSPv peaked at P7 but declined sharply by P16 (Figure 9b), suggesting early transient input from these medial regions. These data suggest that feedback inputs from medial HVAs undergo more dynamic developmental changes compared to those from lateral HVAs.

To understand how reciprocal cortico-cortical connectivity develops, I compared the trajectories of feedforward projections from V1 to higher visual areas (HVAs) with feedback inputs from HVAs to V1 (Figure 9b). Rather than exhibiting tightly coordinated maturation, feedforward and feedback projections for each V1–HVA pair followed distinct developmental courses, with no consistent correlation or anti-correlation across regions. Mature interareal connectivity in the mammalian cortex is often reciprocal, with the strength of projections between two areas approximately balanced in both directions (Markov et al., 2014; Watakabe et al., 2023). While this organizational feature has been documented at both areal and cellular levels across species (Kim et al., 2020; Watakabe et al., 2023; Siu et al., 2021), its developmental origins remain unclear. In my datasets, regions that received strong V1→HVA projections tended to overlap spatially with those sending feedback to V1, suggesting an early emergence of reciprocity (Figure 9c).

To test whether this reciprocity strengthens over time, I compared the spatial profiles of V1 outputs and HVA inputs across ages using Pearson correlation analysis (Figures 3 and 8). This analysis revealed a progressive increase in correlation, from near zero in early development (P3→P6: $r = 0.066$, $p = 0.8775$) to a significant positive correlation in adulthood (P60+→P64+: $r = 0.736$, $p = 0.0373$) (Figure 9d). These findings indicate that while reciprocal architecture is a hallmark of the mature cortex, it emerges gradually through independently timed feedforward and feedback processes.

MAPseq-based high-throughput mapping of individual V1 CCPNs shows that projection motifs are largely comparable across development at the single-cell level

To study the development of long-range axonal targeting at single-cell resolution, I used MAPseq (Kebschull et al., 2016) to examine feedforward axonal projections during three postnatal windows: P14→P16, P22→P24, and P60+→P62+. Earlier developmental stages were excluded from analysis due to overall low levels of axonal projections (Figure 3c) and challenges in reliably micro-dissecting target areas. While bulk anterograde and retrograde tracing of feedforward and feedback connectivity between V1 and HVAs reveals aggregate connectivity, it does not capture how the projections and collaterals of single cells that comprise this aggregate connectivity may be subdivided. To overcome this limitation, I employed MAPseq, a high-throughput barcoding method in which hundreds to thousands of V1 neurons are uniquely labeled following a single injection of a barcoded RNA library. Since barcodes are transported along axons, I dissected five known target areas of V1 CCPNs—RSP, PM, AM, AL, and a combined LM/LI—and sequenced the barcodes in each region to identify projection motifs and quantify projection strengths of individual neurons across development.

To profile MAPseq-labeled axons across three postnatal time points, I quantified total unique molecular identifier (UMI) counts, mean UMI counts per cell, and the number of unique barcodes in the five chosen targets. These metrics in P60+→P62+ brain samples were generally consistent with those from the

VSV-labeled population dataset (Jensen–Shannon divergence values, 0.2597 for the comparison between MAPseq and VSV datasets, and 0.1510 for the comparison between MAPseq and the Allen Brain Projection Atlas datasets, Figures 3 and 15, Table 4). LM/LI consistently showed the highest total and mean UMI counts and barcode diversity, while RSP showed the lowest (Figure 10e). Notably, the mean UMI count in LM/LI decreased from P14→P16 to P22→P24 (one-way ANOVA, $p = 0.0497$, Figure 10e), which resembles the decline observed in VSV-labeled axons in LM and LI from P12→P16 to P20→P24 in the VSV tracing experiments (Figure 3c). In addition, analysis of specific projection motifs (V1→AL, V1→PM, V1→AL+PM) over time revealed that the proportion of V1→AL+PM axons labeled by MAPseq remained consistently low across development (greatest at 8.8% at P14→P16, compared to 6.1% at P60+→P62+), consistent with the low frequency of this motif observed in CTB tracing across developmental and adult stages (Figure 1h). Over time, the proportion of V1→AL projections increased, while V1→PM projections decreased, a trend also seen in the CTB-labeled dataset. In addition, comparison of the P60+→P62+ MAPseq data with a previously published adult dataset revealed similar projection target motifs and strengths (Han et al., 2018) (See Chapter 4: Conclusions). Together, these findings show that developmental MAPseq data aligns well with results from other tracing methods (VSV and CTB), and the adult MAPseq data are comparable with existing adult datasets (Figures 1, 3, 10, and 15b).

To determine whether axonal projection profiles to five target areas change over development, I quantified the number of targets innervated by individual V1

neurons at each age. At P14→P16, approximately 68.1% of MAPseq-labeled neurons projected to one target, 25.6% to two, and 5.6% to three. Similar distributions at P22→P24 (81.3% for one, 16.6% for two, 2.0% for three) and P60+→P62+ (76.3% for one, 19.2% for two, 3.9% for three) were observed, with no significant differences across age groups (one target: $p = 0.5535$; two targets: $p = 0.5535$; three targets: $p = 0.8189$; Kruskal-Wallis test with Dunn's post hoc test, Figure 10f). These results suggest that the number of projection targets per neuron remains largely consistent over time. Likewise, entropy values, measures of projection complexity, were similar across stages (P14→P16 = 0.8567, P22→P24 = 0.8567, P60+→P62+ = 0.8259) (Figure 10g), further indicating that overall projection patterns are not substantially altered during this developmental window.

Next, I examined the diversity and abundance of individual neurons' axonal projection motifs and how they change across development. I analyzed 614 MAPseq-labeled V1 CCPNs from 3 mice at P14→P16, 492 neurons from 3 mice at P22→P24, and 2117 neurons from 7 mice at P60+→P62+. To assess motif specificity, I compared the observed data to a null model in which each neuron projects independently to each target with equal probability and no preference for specific motifs. This analysis revealed a wide range of projection patterns, with certain motifs occurring in a non-random manner in the adult brain, consistent with previous findings (Han et al., 2018) (Figure 10j). I then determined whether the prevalence of specific motifs changed over time. Similar patterns were observed at P14→P16 and P22→P24, although the statistical significance of individual motifs

was generally lower at P22→P24. These results suggest that specific projection motifs are largely maintained throughout development, with no major shifts in their overall representation. This supports the idea that single-neuron axonal output profiles during development resemble those in the adult brain, rather than being reshaped through extensive inter-regional reorganization, consistent with the results from CTB and sequential AAVretro experiments (Figure 1).

Chapter 3: Materials & Methods

Experimental age group notation

Given the variety of tools and incubation times used in this study, I use the following notation throughout this document to describe the period during which any given experiment can be presumed to have begun labeling cells at the time of the injection, and when the final traced circuit was observed following tissue harvest: $PX_{injection} \rightarrow PY_{harvest}$. Examples include: P3→P6, P6→P9, P12→P18, and P60+→P65+. This notation allows direct comparison across tracing modalities and timepoints, and ensures consistency in tracking circuit progression across postnatal development.

Experimental animals and husbandry

C57BL/6J mice (Jackson Laboratory, Stock No. 000664) and transgenic mouse strains maintained on the C57BL/6J background were used for all experiments. Both transgene-negative and transgene-positive animals were included when the presence of the transgene was not expected to affect the outcome. Both male and female mice were used (specific animal sexes where known are listed in Table 1). The specific ages of experimental animals used are described in Table 1. All mice were housed with a 12-hour light and 12-hour dark cycle and *ad libitum* access to food and water. All animal procedures were performed in accordance with the University of California, Santa Cruz animal care and use committee (IACUC)'s regulations.

Virus preparation

All adeno-associated viruses (AAVs) and VSVdG were produced by the Salk Institute GT3 Viral Core: scAAVretro-hSyn-H2B-eGFP (referred as AAVretro-H2B-eGFP, $1.16X10^{13}$ GC/ml), scAAVretro-hSyn-H2B-mCherry (referred as AAVretro-H2B-mCherry, $1.21X10^{13}$ GC/ml), and VSVG+VSVdG-tdTomato ($5.34X10^{10}$ infectious unit/ml). Sindbis viruses were produced by the Cold Spring Harbor Laboratory MAPseq core: Sindbis Virus barcode library expressing eGFP: L2.2 mappnl and vamp2 (~$2.0X10^{9}$ infectious particles/ml).

Animal surgery and injections

For all adult surgeries, anesthesia induction was with either 100 mg/kg of ketamine and 10 mg/kg of xylazine cocktail via intraperitoneal injections, or 3% isoflurane and subsequent maintenance with ~1% isoflurane. Adult mice were mounted in a stereotaxic frame (RWD instruments) for surgery and stereotaxic injections. Stereotaxic injections in adult mice were targeted using the following coordinates: 1.6-1.9 mm rostral, 1.5 mm lateral relative to lambda and 0.4-0.6 mm ventral from the pia for PM, 1.1 mm rostral, 2.6 mm lateral to lambda and 0.4-0.6 mm ventral from the pia for V1, 1.5-2.0 mm rostral, 3.6 mm lateral to lambda and 0.4-0.6 mm ventral from the pia for AL, 0.7-1.0 mm rostral, 3.65 mm lateral relative to lambda and 0.4-0.6 mm ventral from the pia for LM. Injections of all virus types were done using air pressure manually controlled by a 3 ml syringe with 18G tubing adapter and tubing connected directly to the glass injection pipette. To prevent injection backflow, the pipette was left in the brain for 3 minutes after the completion

of the injection. Following recovery, all mice were injected with subcutaneous carprofen (5 mg/kg) and housed with a water bottle containing ibuprofen (30 mg/kg).

For all pup surgeries, anesthesia induction was achieved with 3% isoflurane and subsequent maintenance with 0-3% isoflurane. Animals older than P12 were mounted in a custom restraint frame designed in-house for typical stereotaxic surgeries in pups. Stereotaxic injections in P3 mice were targeted using major blood vessel landmarks and the following coordinates: 1.2 mm rostral from the transverse sinus, 1.0 mm lateral relative to lambda and 0.1-0.25 mm ventral from the pia for PM, 0.7 mm rostral from the transverse sinus, 1.7 mm lateral to lambda and 0.1-0.25 mm ventral from the pia for V1, 1.5 mm rostral from the transverse sinus, 2.45 mm lateral to lambda and 0.1-0.25 mm ventral from the pia for AL, 0.7 mm rostral from the transverse sinus, 2.45 mm lateral relative to lambda and 0.1-0.25 mm ventral from the pia for LM. For ~P12 and ~P20 surgeries, injections were guided by major blood vessel landmarks with post-surgery verifications. Accurate targeting of designated areas was screened prior to data analysis by assessing fluorescence at the injection sites and identifying injection locations using brain atlases and Bell Jar as reference tools.

For cholera toxin subunit B (CTB) tracing experiments, 5–10 nl of CTB conjugated to Alexa Fluor dyes, CTB-647 (1 mg/ml, Invitrogen C34778), CTB-555 (1 mg/ml, Invitrogen C22843), or CTB-488 (1 mg/ml, Invitrogen C34775), was injected into PM and AL, with fluorophore assignment rotated evenly across replicates. Mice were incubated for 3–6 days prior to tissue collection for histology.

For VSVG+VSVdG-tdTomato and AAVretro-H2B-eGFP/mCherry experiments, viruses were injected at the previously described coordinates, followed by a defined incubation period prior to tissue collection. Injection details for individual animals are provided in Table S1.

Tissue collection and histological processing

Tissue was harvested following a defined incubation period (see Table S1) using transcardial perfusion with 1X phosphate-buffered saline (PBS) containing heparin (10 U/ml, Sigma-Aldrich H3393), followed by fixation in 4% paraformaldehyde (PFA). Adult (from P60 to P90) or P20+ brains were immediately dissected from the skull and post-fixed in 2% PFA and 15% sucrose at 4°C overnight. Pup (from P3 to P20) heads were post-fixed in 2% PFA and 15% sucrose at 4°C overnight, after which brains were dissected from the skull and post-fixed again in 2% PFA and 15% sucrose at 4°C overnight.

Following post-fixation, both adult and pup brains were cryoprotected by immersion in 30% sucrose in PBS at 4°C until the tissue sank. Using a freezing microtome (Espredia HM430), brains were embedded in 30% sucrose and coronally sectioned at 50 μm. Sections were collected in cryogen (3:3:3:1 ethylene glycol, glycerol, ddH20, and 10x PBS) for cryoprotection, with half stored at -20°C and the other half washed in 1X PBS with 0.01% sodium azide for further staining and quantification.

Brains injected with CTB or VSVG+VSVdG-tdTomato were sectioned coronally, counterstained with DAPI (4′,6-diamidino-2-phenylindole; ThermoFisher

Scientific Invitrogen D1306), and serially mounted onto glass slides using polyvinyl alcohol mounting medium containing DABCO (PVA-DABCO). Slides were air-dried overnight, then cleaned and stored at 4°C. For a subset of AAVretro-H2B-eGFP/mCherry-injected brains (see Table S1 for animal details), free-floating sections underwent immunohistochemistry to amplify endogenous fluorescence. Sections were incubated overnight at 4°C with goat anti-GFP (1:1000; Rockland 600-101-215, RRID: AB218182) and rabbit anti-dsRed (1:500; Clontech 632496, RRID:AB10013483) primary antibodies in PBS containing 0.5% normal donkey serum and 0.1% Triton X-100. After three 10-minute PBS washes, sections were incubated with Alexa Fluor-conjugated secondary antibodies: Alexa 488 (1:500; Invitrogen A-11055, RRID: AB2534102) or Alexa 568 (1:500; Invitrogen A-10042, RRID: AB2534017). Stained sections were mounted onto subbed slides, air-dried overnight in the dark, cleared in xylene, and coverslipped using Krystalon mounting medium (Sigma-Aldrich 64969). Prepared slides were cleaned and stored at 4°C.

Image acquisition

Tissue sections were imaged using a Zeiss AxioImager Z2 widefield microscope equipped with a 10×/0.45 NA objective (working distance (wd): 2.0 mm). High-resolution tiled images were acquired for each section across relevant fluorophore channels and z-depths, typically using 9 focal planes at 5.5 μm intervals. Scan parameters were optimized per experimental group to maximize signal detection, with consistent settings maintained within each group. For datasets requiring cell counting, imaging parameters were adjusted per animal to facilitate

accurate identification. For comparative feature analyses, fixed imaging settings were applied across all samples. Selected representative images were acquired using a Zeiss LSM 880 confocal microscope with either a 10×/0.45 NA (wd: 2.0 mm) or a 40×/0.95 NA corr (wd: 0.25 mm) objective. Whole-brain overviews were imaged using an Olympus SZX16 stereomicroscope.

Image feature analysis for CTB signal quantification

High-resolution images of DAPI-stained coronal sections were used to manually delineate brain regions. An expert anatomist evaluated each image for distinct structural and cytoarchitectural landmarks, and cortical areas (V1, AL, PM, LM, and RSP) along with their laminar boundaries were outlined individually. Cortical laminae were divided into L1, L2/3 upper, L2/3 lower, L4, L5, L6a, and L6b; some layers (e.g., L2/3 subdivisions or L6 and L6a) were merged if necessary. Injection accuracy was assessed after anatomical annotation, and any samples not meeting criteria were excluded. CTB-labeled neurons were manually counted across all layers and channels, including co-labeled cells, by a single rater to maintain consistency.

Image processing with Bell Jar

Following acquisition, raw fluorescence and DAPI counterstain images were exported as .TIFF files using ZEN 3.1 (blue edition), then maximum projected, reoriented as necessary (rotated/mirrored), and converted to 8-bit grayscale. Each

dataset was aligned to the Allen CCFv3 reference atlas using the Bell Jar pipeline, with manual verification and correction of alignment for each section (Soronow et al., 2025). Axon segmentation and signal quantification were performed using the integrated Bell Jar–RSAT pipeline. AAVretro-H2B-eGFP+ nuclei were detected using Bell Jar's default model (tile size = 320, confidence threshold = 0.1, area cutoff = 100).

Clustering of axon detection mask data

Clustering was performed on the global depth profile dataset, replicating the methods from a previous study (Watakabe et al., 2023). Pairwise distances $(d_{x,y})$ were computed for the profiles such that:

$$d_{x,y} = 1 - r_{x,y} = 1 - \frac{\sum_{i=1}^{n}(x_i - \bar{x})(y_i - \bar{y})}{\sqrt{\sum_{i=1}^{n}(x_i - \bar{x})^2}\sqrt{\sum_{i=1}^{n}(y_i - \bar{y})^2}}$$

where $r_{x,y}$ is the Pearson correlation coefficient, x_i and y_i is the i^{th} element of the x and y depth profiles respectively, and $\bar{x}$ and $\bar{y}$ are the sample means of x and y.

Agglomerative hierarchical clustering was applied via SciPy's linkage function using Ward's method. The objective function minimized herein is given by:

$$\Delta(A,B) = \sum(1 \in (A \cup B) \cdot d(i, \text{centroid}(A \cup B)^2 - \left[\sum(i \in A) \cdot d(i, \text{centroid}(A))^2 + \sum(i \in B) \cdot D(i, \text{centroid}(B))^2\right]$$

where A and B are the clusters to be considered for merging and $d(i, \text{centroid(C)})$ is the correlation-based distance between item i and the centroid of a generic cluster C which represents the increase in the sum of squared distances when clusters A and B are merged. This is consistent with Ward who states in his original article that the generalized agglomerative hierarchical clustering can use any objective function to

minimize, wherein here, the above $\Delta(A, B)$ is used where $d(i, \text{centroid(C)})$is correlation-based distance between item i and the centroid of cluster C (Ward, J.H., Jr., 1963). The resulting clusters were then sorted by mean depth for purposes of visualization.

Thorough analysis of optimal number of clusters was applied for number of clusters 2 through 15 using Silhouette Score (Rousseeuw, P.J., 1987) (k=2), Calinski-Harabasz Score (Calinski and Harabasz, 1974) (k=2), Davies-Bouldin Score (Davies and Bouldin, 1979) (k=2), Within-Cluster Dispersion score (MacQueen, J. B., 1967), where k is the optimum number of clusters for each metric.

Min-max normalization was applied to the depth profiles just prior to visualization with respect to each profile individually in order to better represent the relative distributions. Though normalization was not applied prior to clustering, it should be noted that Pearson's correlation coefficient (the metric used for quantifying distance) is invariant to such transformations since, for random variables X, Y, $X' = a + bX$, and $Y' = c + dY$:

$$\text{Cov}(X', Y') = \text{Cov}(a + bX, c + dY) = \text{Cov}(bX, dY) = bd \cdot \text{Cov}(X, Y)$$

and

$$r_{X',Y'} = \frac{\text{Cov}(X', Y')}{\sigma_{X'}\sigma_{Y'}} = \frac{bd \cdot \text{Cov}(X, Y)}{b\sigma_X \cdot d\sigma_Y} = \frac{bd \cdot \text{Cov}(X, Y)}{bd \cdot \sigma_X d\sigma_Y} = \frac{\text{Cov}(X, Y)}{\sigma_X \sigma_Y} = r_{X,Y}.$$

Thus, such normalization offers a representation which is both more intuitive to interpret and consistent with previous literature as well as is mathematically valid (see Figure 3a).

MAPseq preparation and analysis

Tissue preparation and microdissection strategy

A total of 15–100 nl of barcoded Sindbis virus (Cold Spring Harbor Laboratory MAPseq core), depending on the animal's age (See Table 1), was injected into V1 at postnatal days P15, P23, or P60+ following the procedures described in the 'Animal surgery and injections' section. According to MAPseq protocols, brains were harvested 13, 24, or 48 hours post-injection, rapidly fresh frozen, and stored at –80 °C until microdissection.

Microdissections were performed under an Olympus SZX16 fluorescent dissecting microscope at a stable temperature of -20°C using an aluminum dissection block semi-submerged in a $CaCl_2$ solution containing dry ice. Sections were compared to the Allen CCFv3 by an expert rater and dissected by hand for each region with a scalpel. Collected tissue portions were combined into sample tubes per cortical area from the serial slice dissections.

A secondary microdissection method was developed and used to collect tissue samples from developing brains. Following the fresh harvest of experimental brain tissue samples, specimens were flash frozen to an OCT block and stored at -80°C A specialized reticle was made for an Olympus SZX16 fluorescent dissecting microscope configured for fluorescent dissection. This reticle was a printout of the CCFv3 area borders for all visual cortical areas and retrosplenial cortex as visualized tangential to the posterior aspect of V1 where the viral injections were targeted. This reticle was scaled appropriately using the Olympus SZX16's magnification

adjustment, and centered on V1 using common blood vessel landmarks as well as the fluorescent signal at the injection site. The reticle was further aligned to the midline and the transverse sinus. Tissue punches (Ted Pella, 15112-25/50/10) of diameter 0.25 mm, 0.5 mm, or 1.0 mm were then depth-marked for average cortex thickness and used to collect samples from each cortical area. A clean punch was used for every collection site. Following punched tissue collection, the remaining brain tissue was submerged in 8% PFA and allowed to fix overnight. Cryosectioning was then performed on a freezing microtome at 250 μm per section. The resultant tissue was then DAPI-counterstained and mounted to slides for low magnification imaging and post hoc analysis of the tissue collection.

Microdissected tissues were preserved in TRIzol reagent (ThermoFisher Scientific, 10296-010) and submitted to the Cold Spring Harbor Laboratory MAPseq core facility for downstream processing. RNA extraction, barcoded cDNA library construction, and sequencing were performed using NextSeq High Output PE36 or NovaSeq platforms, following previously established protocols (Kebschull et al., 2016).

Barcode processing and projection mapping

Using the CSHL MAPseq core's python scripts, raw barcode sequencing data were processed into spike-in normalized barcode matrices (nbcm), where rows

represented individual barcoded neurons and columns corresponded to anatomical regions (See code availability for Zador laboratory github).

Using these NBCMs, neuronal projection patterns were analyzed at single-cell resolution using a custom Python-based pipeline described below (See code availability for Kim Lab Code).

Preprocessing individual barcode matrices

Values from the negative control, on a per replicate basis, were averaged and the standard deviation was calculated. A minimum threshold filter was applied to each replicate spike in the normalized barcode matrix in a global fashion using this calculated value (AVGneg+STDdev). Subsequently, all cells containing a non-zero value in their negative control sample were removed. As in previous studies, all age-group specific replicate data was then concatenated into a single barcode matrix for further cohort-level analysis (script used for section, preprocess_and_aggregate.py).

Analysis of cohort level MAPseq datasets

Stringent filtering was applied to the aggregate cohort level data to maximize analysis of "high-confidence" cells. This included a requirement that all target counts be less than their V1 count and that the minimum barcode number at the injection site ($UMIinj \geq 300\ UMI$), a minimum target barcode count in at least one projection area (UMItarget$\geq$10 UMI), and at least a ten-fold difference between the UMIinj and the largest UMItarget on a per cell basis ((UMIinj)$\geq$(10(MAX(UMItarget))). Barcodes

failing to meet these specifications were eliminated from further analysis (script used for section, process-nbcm-tsv.py).

Projection motif identification

Filtered data were used to construct projection profiles by normalizing barcode counts across target regions. Projection motifs were defined as neurons targeting multiple brain regions, with the total number of projections per neuron computed as:

$$Ptotal = r = 1\sum RI(Xr > 0)$$

where Xr represents barcode counts in region r_i, and $I(Xr > 0)$ is an indicator function (script used for section, process-nbcm-tsv.py).

Statistical inference of projection distributions

To estimate the total number of labeled neurons (N_0), let:

$$N0 = \sum r = 1Rln(1 - Pr)ln(1 - Ptotal/N0)$$

where Pr is the probability of a neuron projecting to region r. The probability of observing each projection motif was modeled as:

$$P(M) = pen(1 - pe)(R - n)$$

where n is the number of target regions, and (Pe→pe) represents the probability of a neuron forming a projection to e and pe (script used for section, process-nbcm-tsv.py).

Cluster and motif analysis

K-means clustering was applied to identify distinct projection patterns, with the optimal cluster number determined via the elbow method. Motif occurrence was compared against an expected distribution, with statistical significance assessed using binomial tests:

$$P(X \geq k) = x = k \sum N(xN) px(1 - p)(N - x)$$

where k is the observed count of a given motif, and p is the expected probability of occurrence. Correction for multiple comparisons was performed using Bonferroni-adjusted thresholds (script used for section, process-nbcm-tsv.py).

Visualization and interpretation

Projection data were visualized through heatmaps, t-SNE embeddings, and UpSet plots. Co-targeting probabilities between regions were computed as:

$$P(B|A) = N(A)N(A \cap B)$$

where $N(A \cap B)$ is the number of neurons projecting to both regions, and $N(A)$ is the total number projecting to region A. Projection strengths were compared across neurons to reveal hierarchical projection structures (script used for section, process-nbcm-tsv.py).

Comparison of VSV and MAPseq Data with Allen Brain Institute Connectivity Data

Adult mouse brain connectivity data were obtained from the Allen Brain Institute (ABI) connectivity atlas (IDs: 100141219, 100147853, 277616630, 277712166, 277713580, 277714322, 304564721, 304585910, 304586645,

304762965, 307137980, 307320960, 307557934, 307593747, 309003780, and 309113907). In these datasets, anterograde axon tracing was conducted by stereotaxic injection of AAV1 expressing eGFP into the right hemisphere's V1 region, using iontophoresis (Oh et al., 2014).

The injection hemisphere for each mouse was visually confirmed via the Allen Brain Atlas portal, and raw XML data for each case was downloaded and filtered to the relevant areas. The VSV and MAPseq datasets for our adult mice were similarly reformatted to match ABI structure. For VSV data, the metric used was the quotient of raw axon pixels divided by the number of starter cells in each animal.

For ABI–VSV comparisons, the following eleven areas were used (in lateral to medial order): POR, LI, LM, AL, RL, A, AM, PM, RSPagl, RSPd, RSPv. For ABI or VSV comparisons with MAPseq, areas were collapsed and ordered as: LM+LI, AL, AM, PM, RSP (RSPagl+RSPd).

After standardizing across datasets, each animal's data was averaged by area to produce a single vector of means. To normalize each distribution into a probability vector while preserving relative structure, log-Softmax normalization was applied (Bridle, J., 1989).

Softmax function:

$$\text{Softmax}(z_i) = \exp(z_i) / \Sigma\square \exp(z\square)$$

This is equivalent to the Boltzmann distribution:

$$p_i = \exp(-\varepsilon_i / kT) / \Sigma\square \exp(-\varepsilon\square / kT)$$

when:

$$z_i = -\varepsilon_i / kT$$

Log-Softmax function:

$$\text{log-Softmax}(z_i) = z_i - \log(\Sigma\square \exp(z\square))$$

This formulation helps suppress artificial inflation of small values during exponentiation, preserving the shape of the distribution.

After normalization, we computed Jensen–Shannon divergence (JSD) between each pair of datasets. JSD is a symmetric and bounded measure of similarity between two probability distributions, ranging from 0 (identical distributions) to 1 (maximal divergence).

JSD definition:

$$JSD(P \parallel Q) = \tfrac{1}{2} \cdot D\_KL(P \parallel M) + \tfrac{1}{2} \cdot D\_KL(Q \parallel M)$$

where:

$$M = \tfrac{1}{2}(P + Q)$$

and,

$$D\_KL(P \parallel M) = \Sigma\, P(i) \cdot \log_2[P(i) / M(i)]$$

Because interpretation of JSD values depends on the specific context, and no universal thresholds exist, we generated a reference distribution for each dataset by computing all pairwise JSD values among individual samples (resulting in n^2 values per dataset) (Majtey, Lamberti, and Prato, 2005). This analysis was performed on projection arrays corresponding to LM+LI, AL, AM, PM, and RSP (For all values see Table 4).

The mean JSD for the ABI set was found to be 0.2749 which indicates that this is how different on average any given array for a pair of mice are in the ABI set. When comparing between each set, we have that ABI-VSV = 0.2553, ABI-MAPseq: 0.1510, and VSV-MAPseq: 0.2597 which are all below the mean JSD for the within ABI set.

Kolmogorov-Smirnov p-values were also computed for each pair of datasets for each area (For all values see Table 4).

Quantification and statistical analysis

The values of n and what n represents are reported in the Results section or the figure legends. Statistical analyses were performed using GraphPad Prism 10.1.1 or custom Python scripts. Statistical analyses were selected based on the experimental design and included Student's t-test, chi-square test, one-way ANOVA with uncorrected Fisher's LSD, two-way ANOVA with Tukey's multiple comparisons test, Pearson's correlation, Kruskal-Wallis test with Dunn's post hoc test, among others. The specific tests used are indicated in the Results section or figure legends. Unless

otherwise noted, statistical significance is indicated as follows: *p < 0.05; **p < 0.01; ***p < 0.001; ****p < 0.0001.

Code availability

All code developed in the Kim Laboratory and used in this manuscript is available on the Github project pages, which can be found on the lab website (www.ejkimlab.com/code). Additional MAPseq matrix generation tools can be found at the Zador laboratory github (https://github.com/ZadorLaboratory/mapseq-processing).

Chapter 4: Conclusions & Future Directions

My study reveals that, despite being spatially intermixed, V1 CCPNs establish long-range cortico-cortical connectivity through axonal development programs that are both target-specific and temporally distinct. These differences include variation in both the onset of axon extension and the timing of pruning, yet the overall projection motifs of individual neurons remain largely stable through postnatal development. This indicates that long-range cortical circuits are refined primarily by local remodeling within target areas, rather than large-scale rewiring of projection identity. Specifically, I found that (1) V1→AL and V1→PM projections arise through early, dedicated axon targeting rather than exuberant multi-target outgrowth; (2) medial targets are innervated before lateral ones, revealing a spatiotemporally biased expansion and refinement program; (3) axonal pruning, not apoptosis, underlies the reduction of lateral projections; (4) laminar projection profiles develop in target-specific ways; (5) reciprocal feedback inputs to V1 strengthen gradually over development; and (6) MAPseq tracing confirms that single-cell projection motifs remain largely stable over time.Together, these findings indicate that long-range cortical circuits are refined primarily by local remodeling within target areas, rather than large-scale rewiring of projection identity.

Despite their origin from a single source area, V1 projections to HVAs follow distinct developmental trajectories, underscoring the diversity of circuit refinement even within a single sensory system. By mapping V1 projections across eleven HVAs

during the first three postnatal weeks, this study provides a comprehensive view of long-range circuit formation within a single sensory modality. This aligns with prior studies comparing projection patterns across different sensory and motor systems and highlights the fine spatial and temporal specificity of cortical wiring programs (Klingler et al., 2021). Notably, I identify differential pruning dynamics along the medial-lateral axis relative to V1, pointing to distinct developmental timelines even within a single sensory system.

What determines the distinct developmental trajectories of spatially intermixed CCPNs remains an open question, with both extrinsic and intrinsic factors likely contributing. This is particularly striking given their presumed exposure to shared global cues such as morphogens or axon guidance molecules. The comparable distances from V1 to each HVA suggest that differences in axonal outgrowth timing are not solely dictated by projection length. While the areal layout and cortical architecture of the visual system have been well characterized (Garrett et al., 2014; Watakabe and Hirokawa, 2018), the role of subcortical pathways and microenvironmental variation in shaping axonal trajectories is poorly understood. Environmental factors—including some features of the white matter, deep gray matter tracts, or local tissue substrates—may differentially influence axonal navigation, although this remains unexplored.This suggests that intrinsic factors, such as gene expression profiles, soma positions within the cortical layer, or neurogenesis timing, may contribute to target-specific connectivity programs. Previous work has shown that subsets of CCPNs, for example V1→AL and V1→PM neurons occupy different

positions within L2/3 and exhibit gene expression differences, and furthermore, that sub-layers of L2/3 exhibit developmental gene expression gradients (Kim et al., 2020; Cheng et al., 2022). Given the inside-out pattern of cortical development, it will be important to determine whether these subpopulations differ in birthdate and how this might influence their axonal growth trajectory.

In addition to intrinsic programs, my findings raise the possibility that target-derived molecular cues or activity-dependent mechanisms contribute to the temporal regulation of V1 CCPN axonal refinement. The observed differences in pruning timing across visual areas may reflect target region-derived trophic factors or local patterns of neuronal activity (Yasuda et al., 2021). Interestingly, dorsal stream HVAs (AL, PM, RL, AM) have been reported to exhibit more delayed maturation of visual receptive properties compared to ventral stream areas (LM and LI) (Smith et al., 2017; Murakami, Matsui, Uemura, and Ohki, 2022). Binocular enucleation at birth has been shown to reduce V1 to HVA connectivity and the number of HVA targets in the mouse visual cortex (Murakami, Matsui, Uemura, and Ohki, 2022). These findings raise the possibility that differences in the anatomical development of V1–HVA connectivity may be linked to differential functional maturation across HVAs, potentially mediated by activity-dependent interactions between V1 CCPNs and their HVA targets. Moreover, recent whole-brain transcriptomic studies in visually deprived or enucleated mice have shown altered expression of cell adhesion molecules, axon guidance cues, and morphogens, suggesting experience and environmental factors may drive gene regulation–mediated changes in connectivity

(Cheng et al., 2022; Chen et al., 2024). Investigating how these molecular signals vary across HVAs and interact with activity patterns during connectivity development will be essential for uncovering the mechanisms that establish target specificity.

My results also prompt broader questions about how axonal selection and synaptic competition shape circuit refinement. For instance, in regions like LM where some projections are maintained and others are pruned (Figure 3), what determines which axons are stabilized? Is synaptic engagement a prerequisite for retention, as seen in neuromuscular and cerebellar systems (Katz and Shatz, 1996)? Addressing these questions will require synaptic-resolution approaches, including axonal imaging with synaptic markers or trans-synaptic tracing to identify functionally integrated axons during development.

In contrast to the dynamic postnatal remodeling observed in feedforward V1 CCPN axons projecting to HVAs, I did not detect asynchronous changes in the number or spatial distribution of feedback input neurons from different HVAs to V1. The notable exception was a prominent early peak in input from medial areas (PM and RSPs) at P7, followed by a sharp reduction by P16 (Figures 5, 6). Although it is important to recognize that quantifying labeled axon pixels and counting neuronal somas reflect fundamentally different aspects of connectivity, as individual neurons can vary greatly in the extent of their axonal arborization (Liu et al., 2024), direct comparisons should be interpreted with caution. Nevertheless, it is noteworthy that V1 CCPNs exhibit earlier axonal innervation of medial HVAs (PM and RSPs), which

coincides with an initially higher number of feedback input neurons from these same areas (Figures 5, 6). In the adult cortex, L5 neurons projecting from V1 to PM are more abundant compared to those in other layers, suggesting a layer-specific enrichment that may contribute to the early development of reciprocal connections between V1 and medial HVAs. This early maturation of V1–medial HVAs connectivity may support behaviorally relevant functions during early postnatal stages. For instance, interactions between V1 and RSPs could play a role in sensory-cognitive roles related to pup behaviors such as locating the dam's nipples for suckling shortly after eye opening (Robinson et al., 2012).

To examine how individual V1 CCPNs establish and refine their axonal outputs across development, I applied MAPseq to profile projection motifs at single-cell resolution across three postnatal stages. The proportion of neurons projecting to one, two, or three targets remained stable from P14 to adulthood, and projection entropy did not increase over time, indicating that axonal output complexity is largely predetermined by early postnatal stages. Consistent with bulk tracing data, AL+PM dual-target projections were rare at all ages, supporting the conclusion that dedicated motifs are established early and maintained through development. These findings align with a prior adult MAPseq study (Han et al., 2018), which similarly identified AL+PM as an under-represented motif and reported substantial proportions of both dedicated and broadcasting V1 CCPNs. Compared to that study, my data revealed a slightly higher proportion of single-target motifs and a lower proportion of multi-target motifs, potentially reflecting differences in target set:

I combined LM and LI due to anatomical ambiguity and included RSP—a non-visual target not present in the earlier dataset—while excluding RL, which is difficult to dissect reliably in developing brains. Despite these minor methodological differences, both datasets reveal stable motif distributions across development and emphasize the coexistence of dedicated and broadcasting projection strategies in the mature cortex.

Together, my findings support a model in which cortico-cortical projection neurons establish long-range connectivity through early, target-specific axon guidance rather than widespread, exuberant outgrowth followed by large-scale pruning. Across multiple tracing methods and developmental stages, I observed that V1→HVA projections are initiated with high specificity, show minimal overlap across target areas, and maintain stable projection motifs at the single-cell level. While postnatal refinement clearly occurs—especially in the form of laminar reorganization and regionally tuned pruning—these changes act locally on already committed projections rather than reshaping projection identity. This trajectory is incompatible with a model of simple pan exuberance and pruning. Instead my research findings support a developmentally programmed, direct guidance mechanism by which CCPNs navigate to and maintain connectivity with their appropriate targets. This framework not only clarifies how stable yet diverse cortical circuits are assembled but also provides a foundation for understanding how disruptions to early axon guidance might underlie connectivity defects in neurodevelopmental disorders.

Collection of Figures

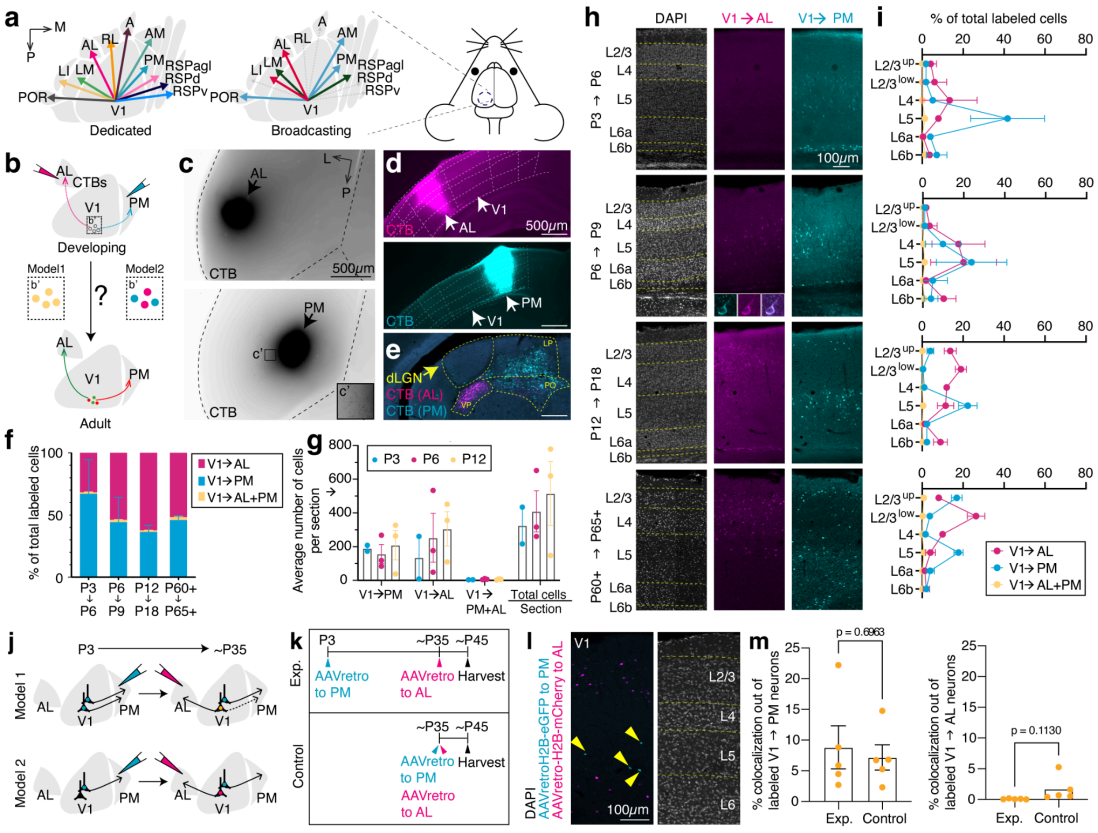

Figure 1. Directed axonal projection from V1 to higher visual areas (HVAs), AL and PM, during development.

(a) Schematic illustrating two modes of long-range axonal projection from V1 to HVAs in the adult brain. In the dedicated model, CCPNs (arrows) project to a single HVA target area. In the broadcasting mode, CCPNs (arrows) extend axons to multiple HVAs in distinct patterns. **(b)** Strategy for projection-based neuronal labeling using fluorophore-conjugated cholera toxin subunit B (CTB) to differentiate between two V1→AL and V1→PM projection models across developmental time points. **(c)** Dorsal view of P6 brains showing precise CTB injections into AL (top) and PM (bottom). **(c′)** Magnified view of the inset location for CTB-labeled V1→PM CCPNs (black). **(d)** Representative confocal images of coronal sections from a P6 brain showing selective CTB labeling in AL (magenta) and PM (cyan) without spillover into V1. **(e)** A confocal image showing the absence of CTB-labeled neurons in the dorsal lateral geniculate nucleus (dLGN; yellow) and the presence in the lateral posterior nucleus needs a label on figure (LP), confirming selective AL and PM targeting at P3. **(f)** Quantification of singly labeled V1→AL (magenta), V1→PM (cyan), and dual-labeled V1→AL+PM (yellow) CCPNs across developmental stages.

(g) Average number of CTB-labeled CCPNs per section over developmental time. **(h–i)** Confocal images and laminar distributions of CTB-labeled V1→PM (cyan) and V1→AL (magenta) CCPNs at different developmental stages. **(j)** Schematic of two models for temporally distinct V1→AL and V1→PM axonal projection development. **(k)** Viral strategy using AAVretro to distinguish between these models in **j**. **(l)** Confocal images showing AAVretro-labeled nuclei of V1→AL and V1→PM CCPNs in V1 at P45. **(m)** Quantification for proportions of double-labeled neurons out of labeled V1→PM (left, P = 0.6963) and V1→AL (right, P = 0.1130) neurons between experimental (Exp.) and control groups. Student's t tests. ns = not significant. For CTB experiments, n = 2 mice for P3→P6, n = 3 for P6→P9, n = 3 for P12→P18, and n = 3 for P60+→P65+. For AAVretro experiments, n = 5 mice for P3→P35→P45 Exp. group and n = 5 for P35→P45 control group. Data are represented as mean ± SEM. Normalization to percentage of total cells was done on a per animal basis where applicable.

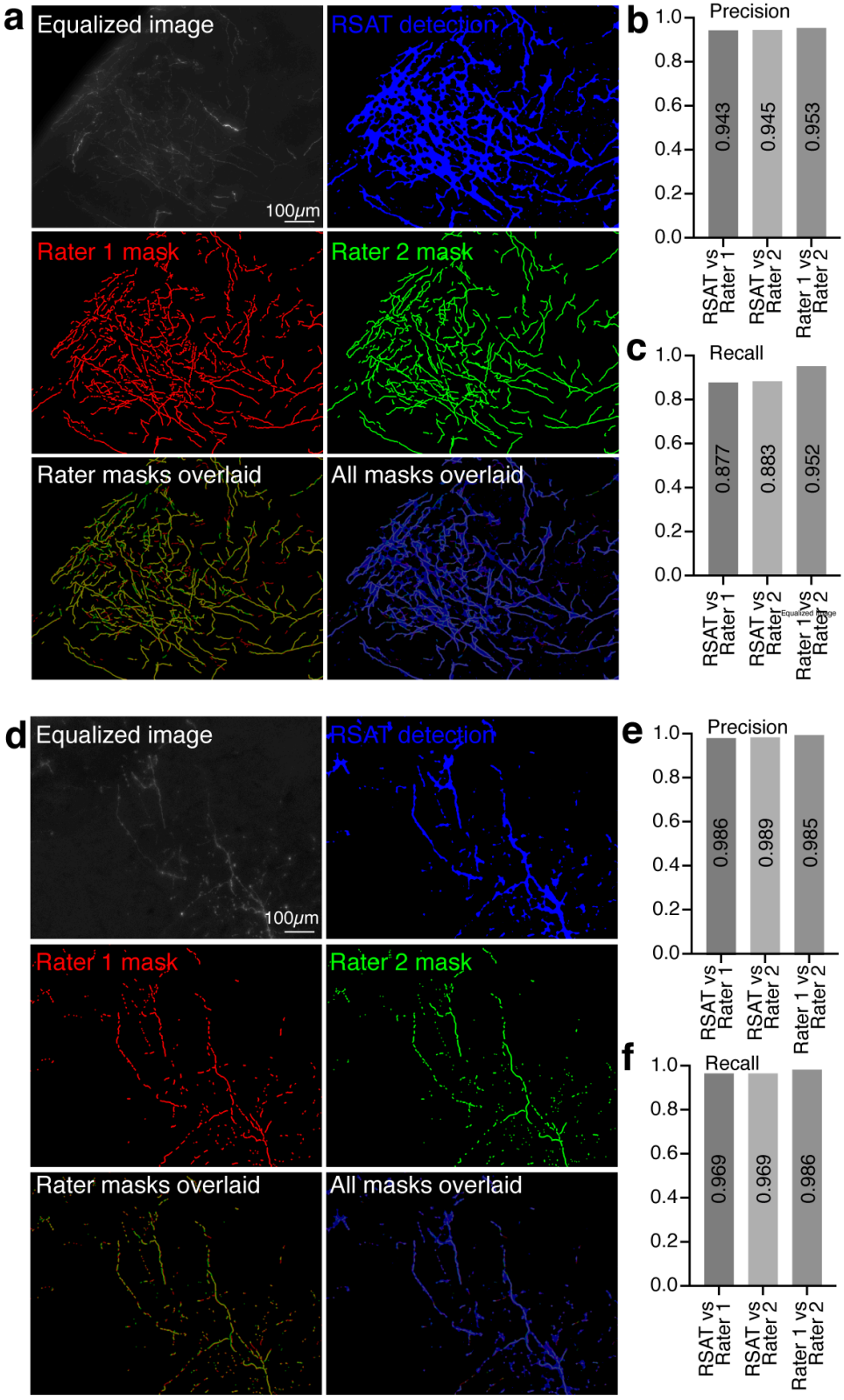
a
Equalized image
100μm
RSAT detection
Rater 1 mask
Rater 2 mask
Rater masks overlaid
All masks overlaid
b
Precision
1.0
0.8
0.6
0.4
0.2
0.0
0.943
0.945
0.953
RSAT vs Rater 1
RSAT vs Rater 2
Rater 1 vs Rater 2
c
Recall
0.877
0.883
0.952
d
e
0.986
0.989
0.985
f
0.969
0.969
0.986

Figure 2. Validation of the Bell Jar-RSAT automated axon quantification pipeline in comparison to expert human raters.

(a, d) Representative fluorescence images showing dense **(a)** and sparse **(d)** tdTomato-labeled axons, displayed as equalized raw images alongside corresponding RSAT automated detection masks and manual annotations by Rater 1 and Rater 2. **(b-c, e-f)** Precision and recall metrics comparing RSAT performance to that of Rater 1 and Rater 2 across both dense and sparse axon labeling conditions.

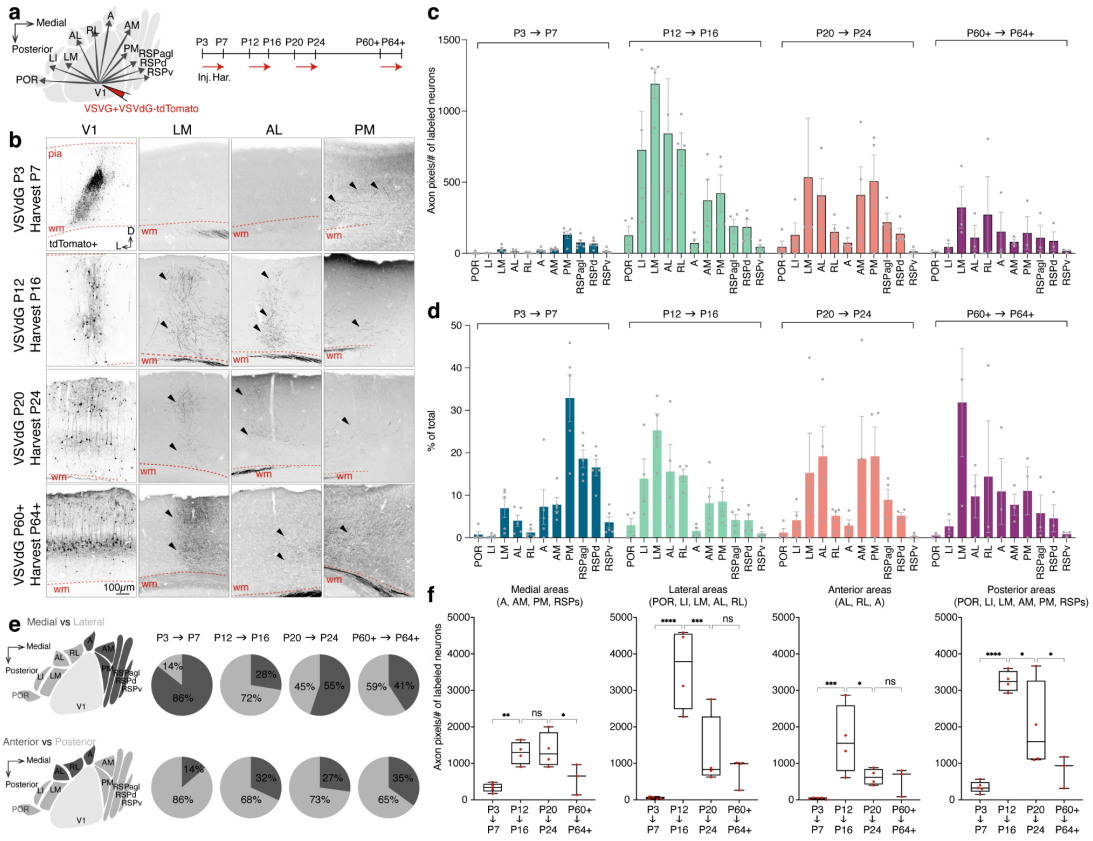

Figure 3. Reconstruction of long-range axonal projections from V1 to eleven cortical areas across postnatal stages.

(a) Schematic of the experimental strategy. VSVG+VSVdG-tdTomato was injected into the center of V1 at various developmental and adult time points. Brains were collected 4 days post-injection for analysis. **(b)** Representative confocal images of coronal brain sections showing V1 injection sites and tdTomato+ neurons (leftmost column) and tdTomato+ long-range axons (arrows) projecting to multiple HVAs: LM, AL, and PM. **(c-d)** Quantification of axonal labeling in 11 cortical areas across development. **(c)** tdTomato+ axon pixel counts normalized per labeled V1 CCPN, and **(d)** the percentage of total tdTomato+ axonal output represented in each area. **(e)** Pie charts illustrating the distribution of tdTomato+ axons in medial versus lateral HVAs (top) and anterior versus posterior HVAs (bottom) at different developmental and adult stages. **(f)** Comparative analyses of tdTomato+ axon pixels per labeled V1 CCPN across developmental stages in medial, lateral, anterior, and posterior target groups. n = 5 mice for P3→P7, n = 4 for P12→P16, n = 4 for P20→P24, and n = 3 for P60+→P64+. one-way ANOVA with uncorrected Fisher's LSD; *p < 0.05, **p < 0.01, ***p < 0.001, ****p < 0.0001. Data are shown as mean ± SEM.

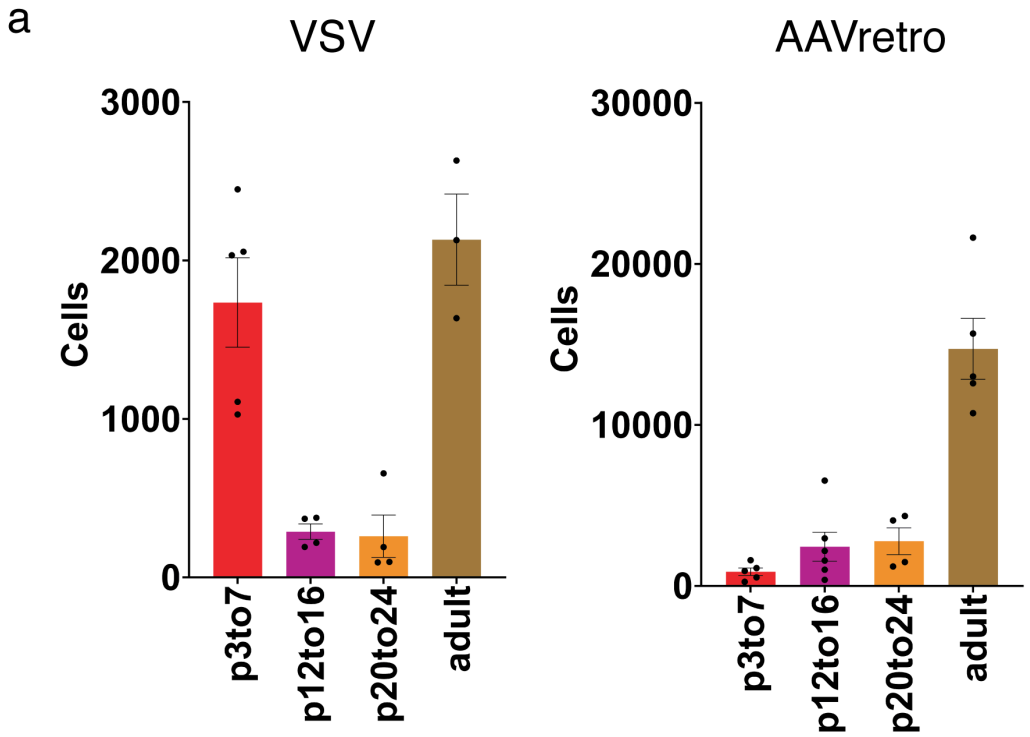

Figure 4. Quantification of viral infection sites

(a) Bar plot for the quantification of VSV infected cells per replicate across age groups. n = 5 mice for P3→P7, n = 4 for P12→P16, n = 4 for P20→P24, and n = 3 for P60+→P64+. **(b)** Bar plot for the quantification of AAVretro-H2B-eGFP infected cells locally at the injection site. n = 5 mice for P3→P7, n = 6 for P12→P16, n = 4 for P20→P24, and n = 5 for P60+→P64+. Data are presented as mean ± SEM.

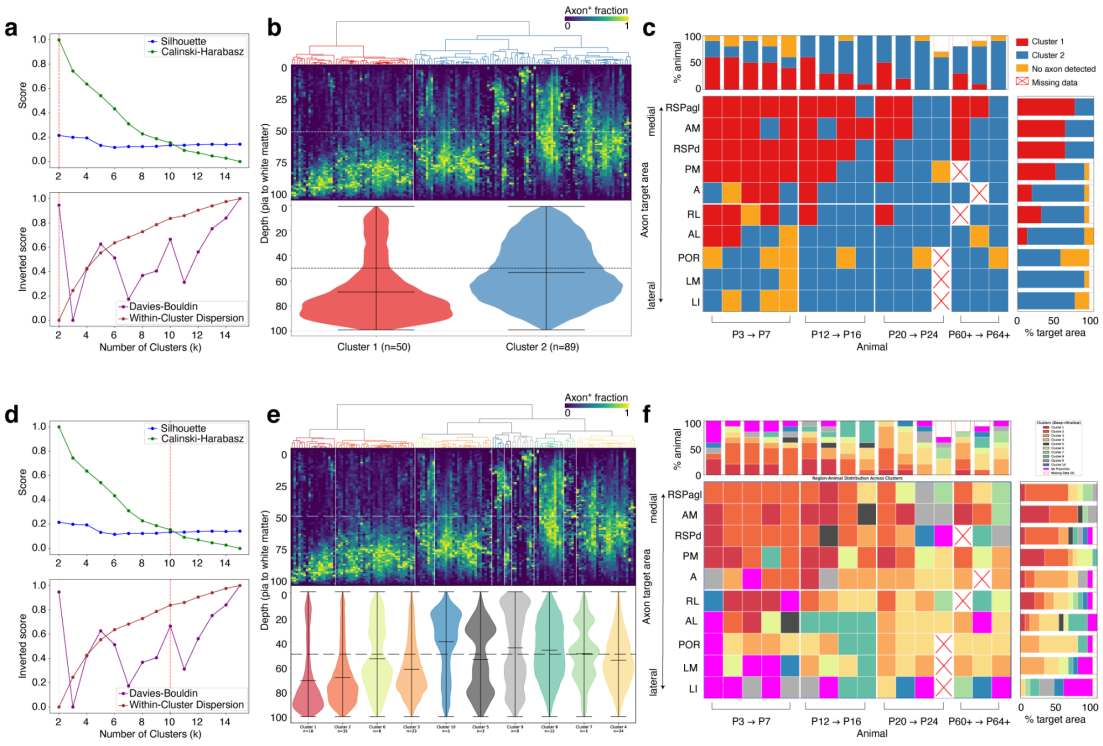

Figure 5. Spatiotemporal dynamics of axon distribution profiles in V1 CCPN target areas across development.

(a) Evaluation of clustering performance using multiple metrics—Silhouette score, Calinski-Harabasz index, Davies-Bouldin index, and within-cluster dispersion for V1 CCPN target areas. The dotted red lines indicate the selected number of clusters (k = 2). **(b)** Hierarchical clustering of V1 CCPN target areas across developmental and adult stages using the Ward's method and Pearson's correlation coefficient as the distance metric, based on axon fraction profiles measured along the pia-to-white matter axis. Violin plots show axon distributions across cortical depth for each cluster. **(c)** Developmental shifts in cluster assignment for 10 cortical areas targeted by V1 CCPNs, revealing spatiotemporal changes in laminar axon profiles. **(d-f)** data clustered into ten groups based on secondary consensus.

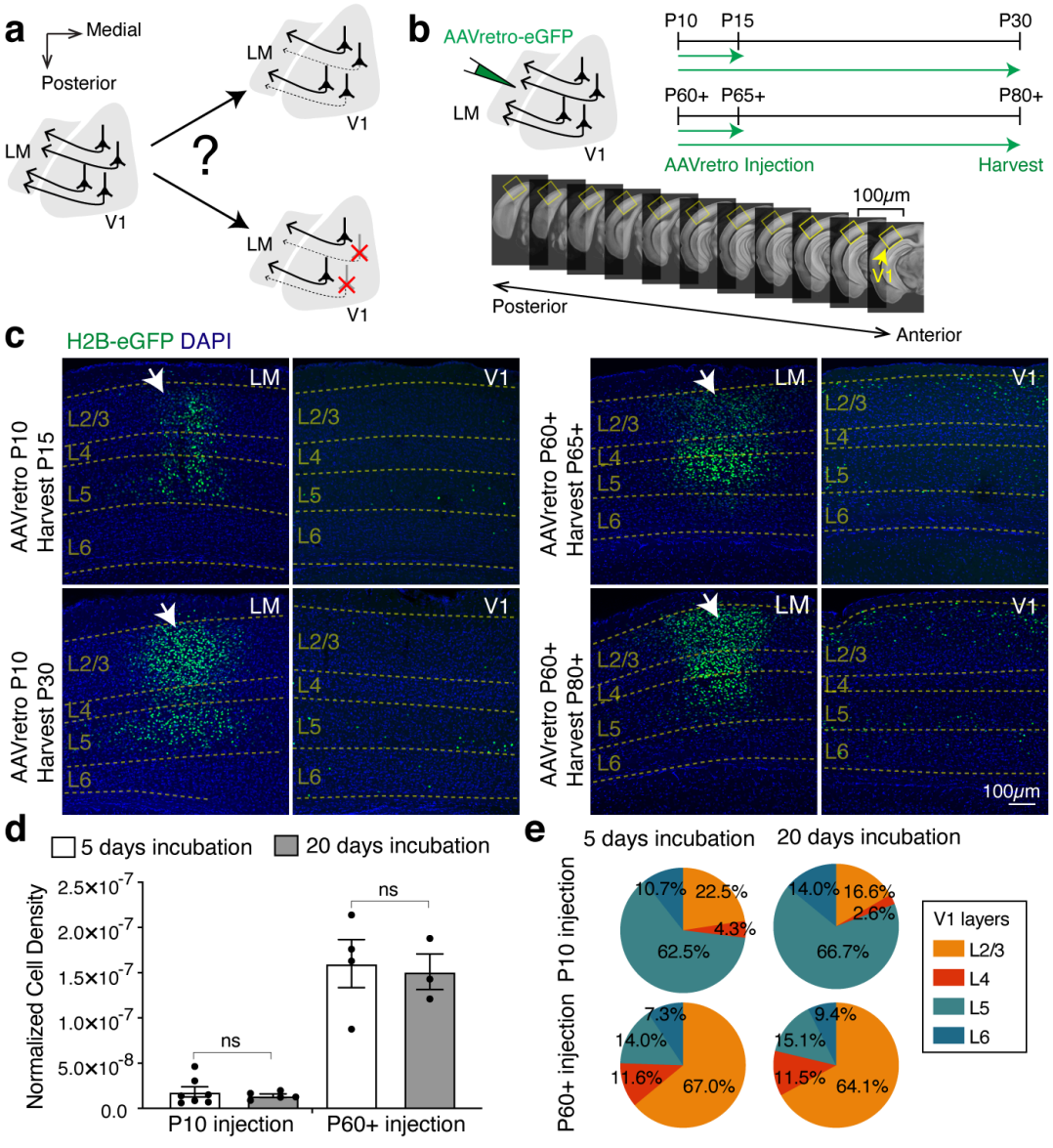

Figure 6. Axonal pruning, rather than apoptosis, underlies the reduction of laterally projecting V1 axons during the second postnatal week.

(a) Two conceptual models illustrating potential mechanisms of axon reduction in lateral V1 projections: axonal pruning (top) versus neuronal apoptosis (bottom). **(b)** Schematic of the experimental design. Top left: AAVretro-H2B-eGFP was injected into LM to label V1→LM neurons retrogradely. Top right: Timeline of viral injection and brain collection at various developmental and adult stages. Bottom: Sequential coronal images across the anterior-posterior axis of the mouse V1 used for whole-region analysis (adapted from the Allen Brain Common Coordinate

Framework) (Wang et al., 2020). **(c)** Representative confocal images showing local H2B-eGFP+ infections (white arrows, left columns) on LM injection sites, along with retrogradely labeled H2B-eGFP+ CCPN nuclei (green) in V1. **(d)** Quantification of V1→LM cell nuclei, normalized to V1 volume, viral labeling efficiency, and brain growth in P30 brains after 20-day viral incubation. **(e)** Pie charts showing the laminar distribution of H2B-eGFP+ CCPN nuclei in V1 for four different experimental groups: P10→P15, P10→P30, P60+→P65+, and P60+→P80+. n = 7 mice for P10→P15, n = 5 for P10→P30, n = 4 for P60+→P65+, and n = 3 for P60+→P80+. Student's t-test; ns = not significant. Data are presented as mean ± SEM.

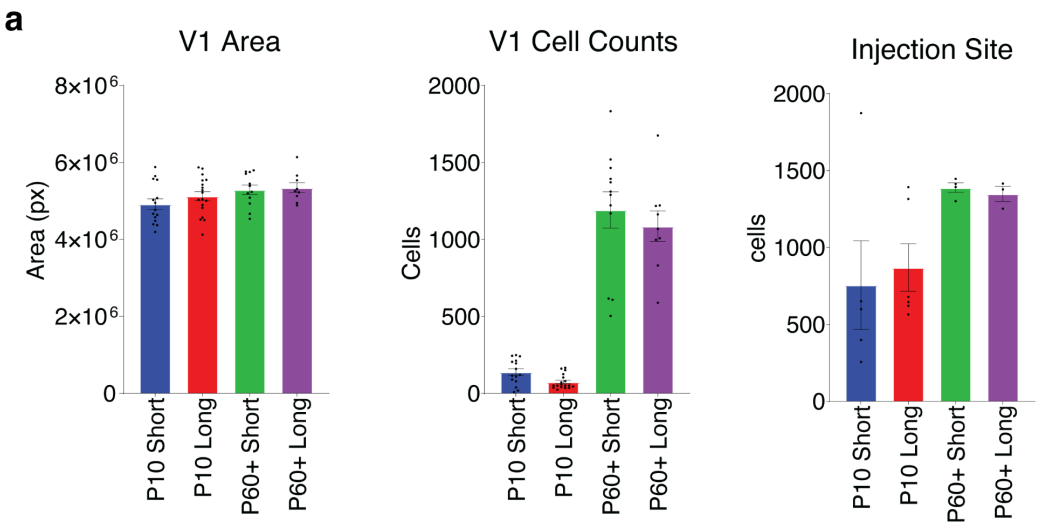

Figure 7. Raw Quantification data for Fig 6d

(a) Raw counts for V1 area in pixels, cell counts across quantified sections, and local cells in the most dense injection site image per animal. For each replicate, three representative serial images were quantified for V1 area and cell counts, as well as a single injection site image (P10 short n = 5, P10 long n = 6, P60+ short n = 4, P60+ long n = 3.).

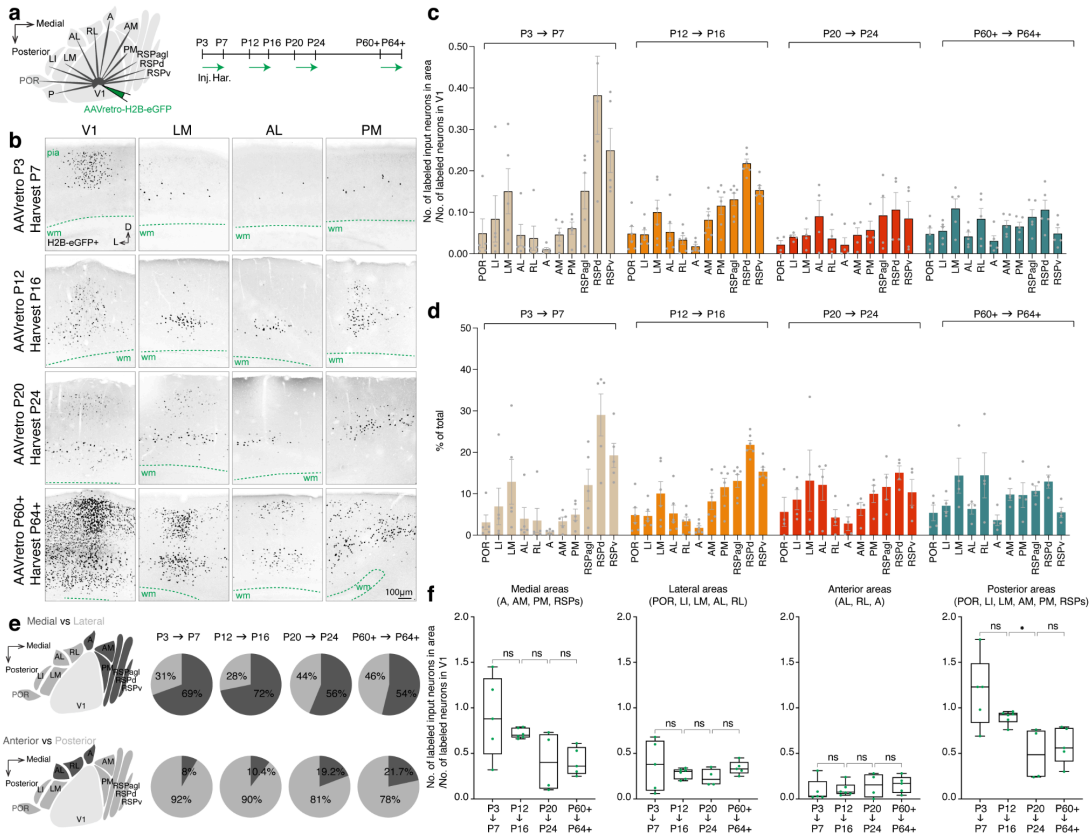

Figure 8. Reconstruction of long-range input neurons from 11 cortical areas to V1 across postnatal stages.

(a) Experimental design: AAVretro-H2B-eGFP was injected into the center of V1 at various developmental and adult stages. Brains were collected 4 days post-injection for analysis of retrogradely labeled input neurons. **(b)** Representative confocal images of coronal brain sections showing locally infected H2B-eGFP+ neurons on V1 injection sites (leftmost column), along with retrogradely labeled H2B-eGFP+ input neurons in selected HVAs: LM, AL, and PM. **(c-d)** Quantification of input neurons across 11 cortical areas throughout development: **(c)** Number of H2B-eGFP+ neurons in each input area normalized to the number of labeled neurons in V1; **(d)** Percentage of total labeled input neurons attributed to each area. **(e)** Pie charts showing the distribution of H2B-eGFP+ input neurons in medial versus lateral (top) and anterior versus posterior (bottom) input areas at different developmental and adult stages. **(f)** Comparative analyses of normalized input neuron numbers across developmental stages in medial, lateral, anterior, and posterior input area groups. n = 5 mice for P3→P7, n = 6 for P12→P16, n = 4 for P20→P24, and n = 5 for P60+→P64+. one-way ANOVA with uncorrected Fisher's LSD; ns = not significant, *p < 0.05. Data are presented as mean ± SEM.

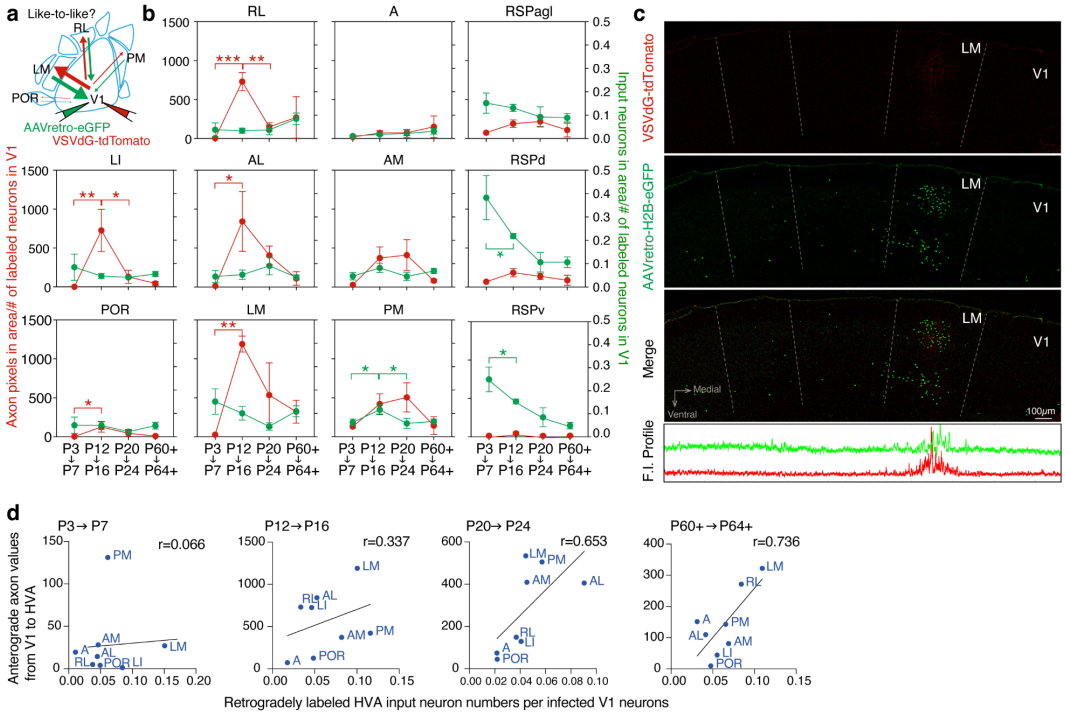

Figure 9. Correlative analysis of connectivity between V1 and HVAs reveals the gradual emergence of like-to-like reciprocal connectivity across development.

(a) Schematic summarizing the experimental datasets used for correlation analysis between V1→HVAs and HVAs→V1connectivity across development. **(b)** Time course quantification of V1→HVAs axon outputs (red, detected axon px/starter) and bulk HVAs→V1 (green, labeled cells in HVAs/labeled V1 cells at injection site) detected in various target areas at different postnatal stages. One-way ANOVA with uncorrected Fisher's LSD test. *p < 0.05, **p < 0.01, ***p < 0.001. Data are presented as mean ± SEM.**(c)** Representative confocal images showing colocalization of local V1 axons (tdTomato+) and input neurons (H2B-eGFP+) in LM. Fluorescence intensity profiles of tdTomato and H2B-eGFP signals along the lateral-medial axis of a coronal section (bottom). **(d)** Pearson's correlation coefficients (r) between V1→HVAs and HVAs→V1 across development. Pearson's correlation of averages by area, P3→P7: r=0.0655 r^2=0.0043, P12→P16: r=0.3366 r^2=0.1133, P20→P24: r=0.6533 r^2=0.4269, P60+→P64+: r=0.7363 r^2=0.5421). Sample sizes for V1→HVA axons: n = 5 mice for P3→P7, n = 4 for P12→P16, n = 4 for P20→P24, and n = 3 for P60+→P64+. Sample sizes for HVA→V1 input neurons: n = 5 mice for P3→P7, n = 6 for P12→P16, n = 4 for P20→P24, and n = 5 for P60+→P64+.

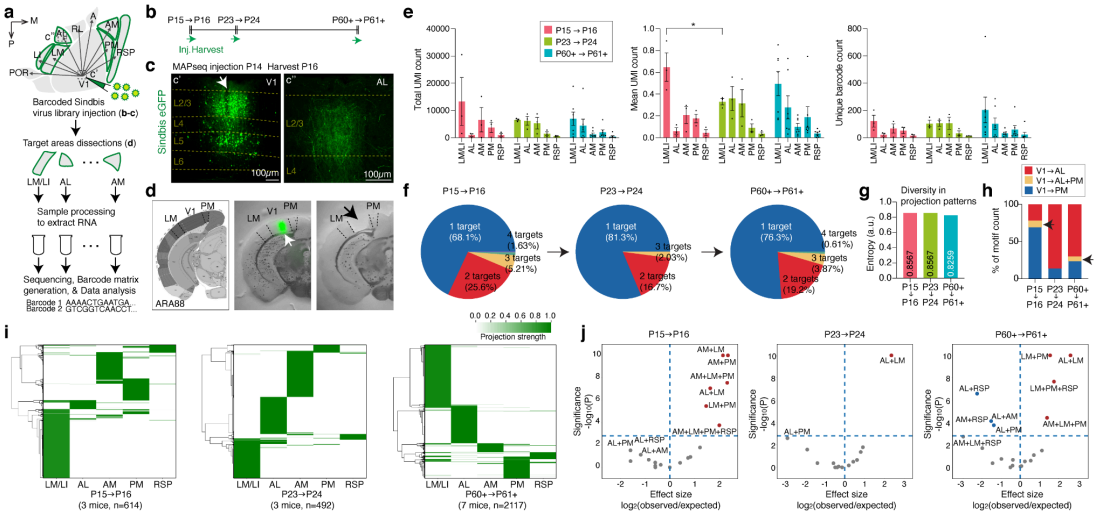

Figure 10. High-throughput, single-neuron resolution analysis of axonal projection pattern development using MAPseq.

(a) Experimental design for MAPseq. A barcoded Sindbis virus library was injected into the center of V1 at various developmental and adult time points. Brains were collected 24 hours later, and target regions, including LM/LI, AL, AM, PM, RSP, and the cerebellum (as a negative control), were microdissected. Tissue samples were processed for RNA extraction, followed by Illumina sequencing and barcode matrix generation for projection pattern analysis. **(b)** Timeline of viral injection and brain collection at various developmental and adult stages. **(c)** Confocal images showing eGFP+ barcoded Sindbis virus injection into V1 at P14 (arrow, left) and eGFP+ barcoded axons in a representative target region, AL (right). **(d)** Example of a Sindbis eGFP-labeled V1 region (white arrow) from a coronal section before (middle) and after (right) microdissection (black arrow). This section's cortical areas - LM, V1, and PM - correspond to those of the ARA88 section from the Allen Brain Common Coordinate Framework (Wang et al., 2020). **(e)** UMI sum (left), UMI mean (middle), and barcode sum (right) for individual animals across three developmental stages. n = 3 mice for P14→P16, n = 3 for P22→P24, and n = 7 for P60+→P62+. One-way ANOVA with uncorrected Fisher's LSD. $p < 0.05$. Data are shown as mean ± SEM. **(f)** Pie charts showing the distribution of neurons projecting to 1–4 targets in each age group (P14→P16, P22→P24, P60+→P62+). **(g)** Diversity of projection patterns measured at different developmental stages. **(h)** Proportion of neurons showing specific projection motifs (V1→AL, V1→PM, V1→AL+PM) across age groups. **(i)** Heatmaps of projection strength from barcoded neurons to five targets, measured by MAPseq at three postnatal stages. **(j)** Volcano plots showing statistical significance and effect sizes for over- and under-represented projection motifs across developmental stages. See Methods for null model generation. n = 614 cells, 5 mice (P14→P16), 492 cells, 3 mice (P22→P24), 2117 cells, 7 mice (P60+→P62+). Detailed cell counts per motif, p-values, and effect sizes are provided in Table 5.

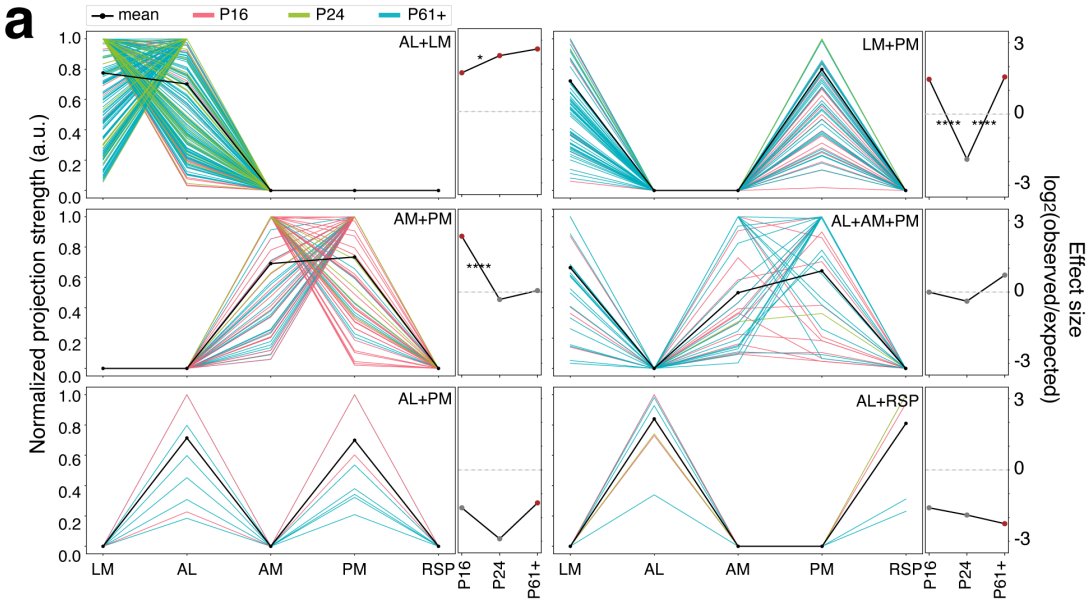

Figure 11. Projection strengths of individual MAPseq-labeled neurons and their developmental changes across three postnatal stages.

(a) Projection strengths of individual neurons for six representative projection motifs across three developmental time points. P14→P16 neurons (red), P22→P24 neurons (green), and P60+→P62+ neurons (blue). Right columns show developmental changes in effect sizes for the same six motifs, which are either over- or under-represented. *p < 0.05 and ****p < 0.0001. Statistical details are provided in Table 6.

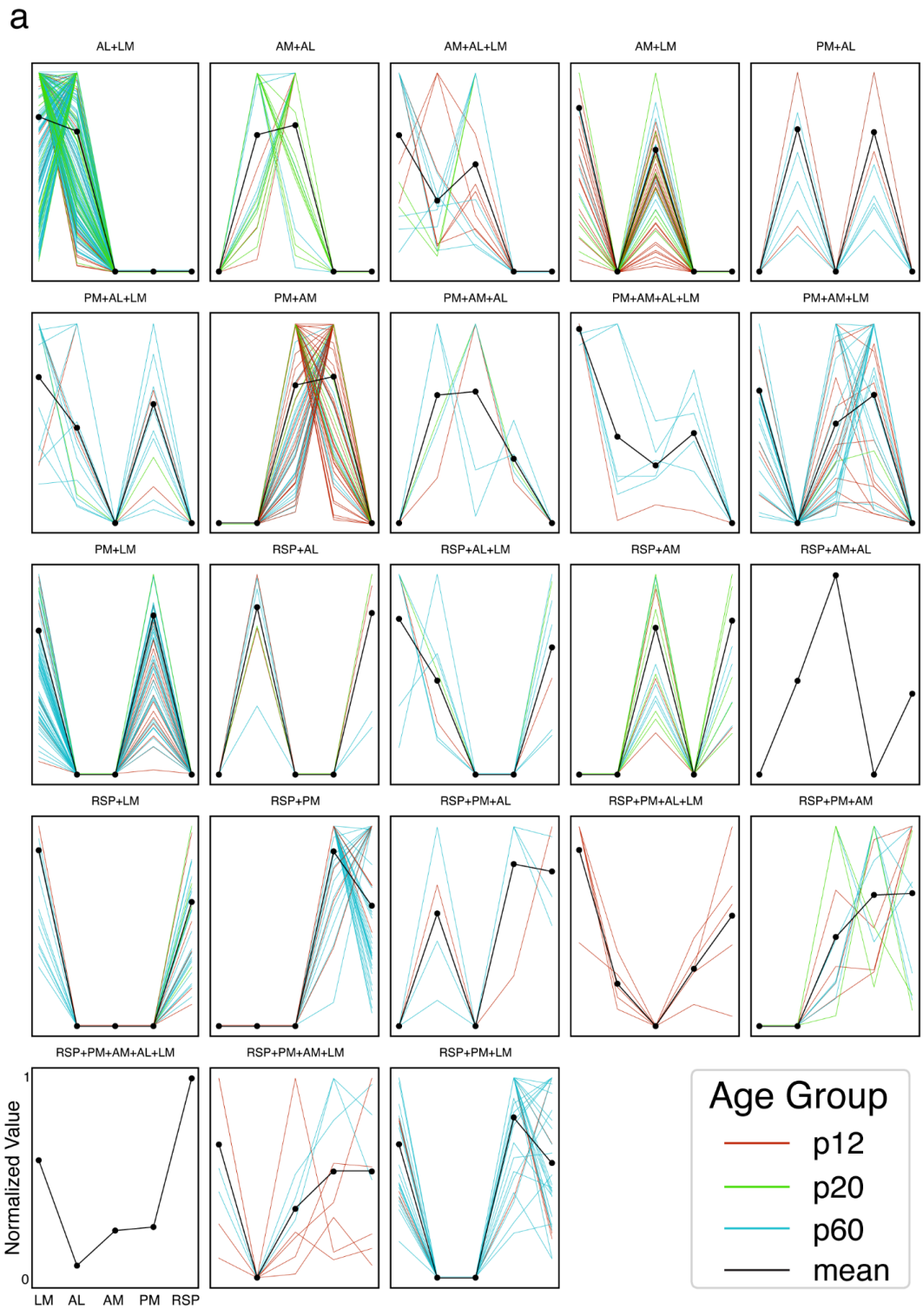
a
AL+LM
AM+AL
AM+AL+LM
AM+LM
PM+AL
PM+AL+LM
PM+AM
PM+AM+AL
PM+AM+AL+LM
PM+AM+LM
PM+LM
RSP+AL
RSP+AL+LM
RSP+AM
RSP+AM+AL
RSP+LM
RSP+PM
RSP+PM+AL
RSP+PM+AL+LM
RSP+PM+AM
RSP+PM+AM+AL+LM
RSP+PM+AM+LM
RSP+PM+LM
Normalized Value
1
0
LM AL AM PM RSP
Age Group
p12
p20
p60
mean

Figure 12. Comprehensive dataset of projection strengths from individual MAPseq-labeled neurons, showing developmental changes across projection motifs and three postnatal stages.

(a) Row normalized projection strengths of individual neurons for 23 representative motifs at three developmental time points: P14→P16 (red), P22→P24 (green), and P60+→P62+ (blue). Black points indicate the mean projection strength for each target area. Soft max normalization done on a per-row basis to visualize the relative projection strength of each neuron to each of its targets (see methods).

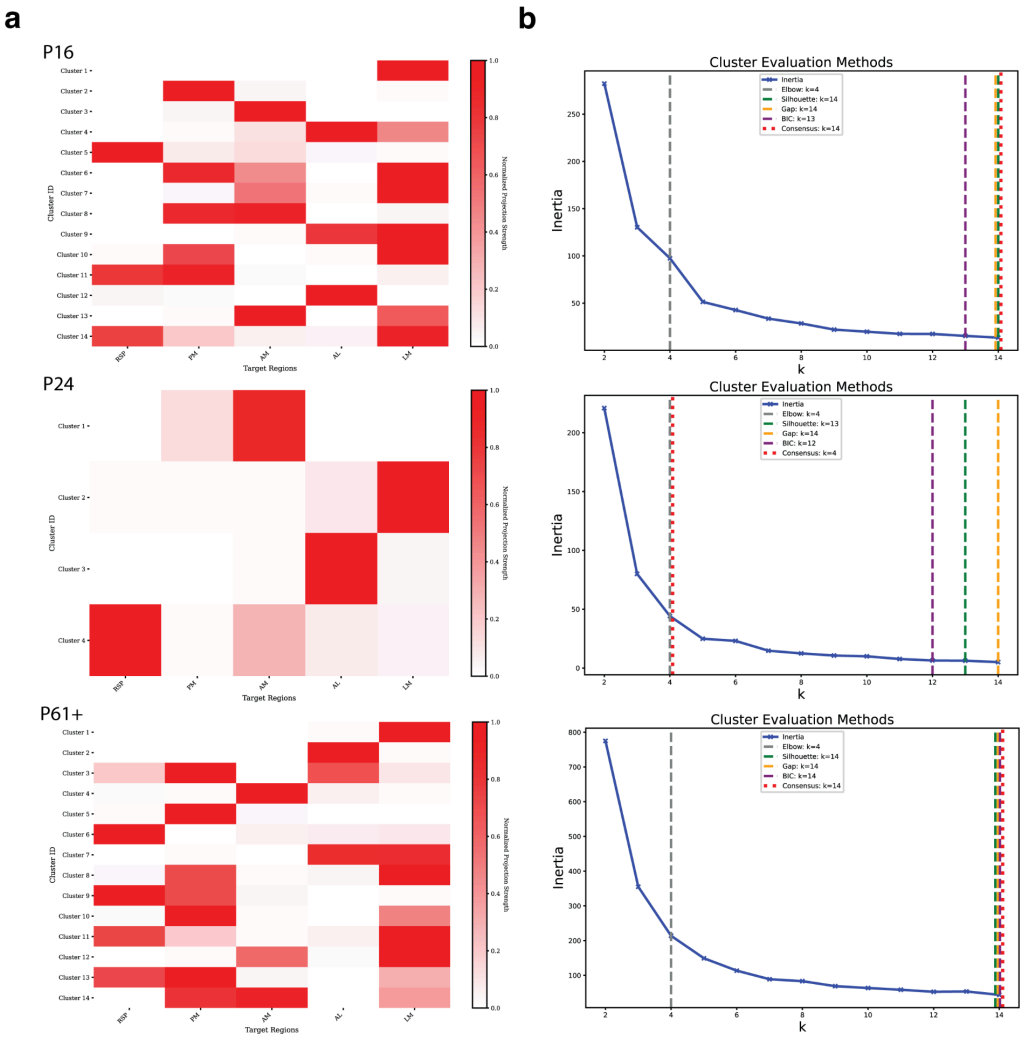

Figure 13. K-Means cluster analysis of MAPseq projection motifs across developmental stages.

(a) Heatmaps showing k-means clustering results based on normalized projection strengths to five target regions at three developmental stages: P14→P16, P22→P24, and P60+→P62+. **(b)** Cluster evaluation using four methods (Elbow, Silhouette, Gap Statistic, and Bayesian Information Criterion (BIC)) to determine the optimal number of clusters for each age group, with the consensus estimate indicated (red dotted lines = at least two values in agreement, else default to the Elbow method).

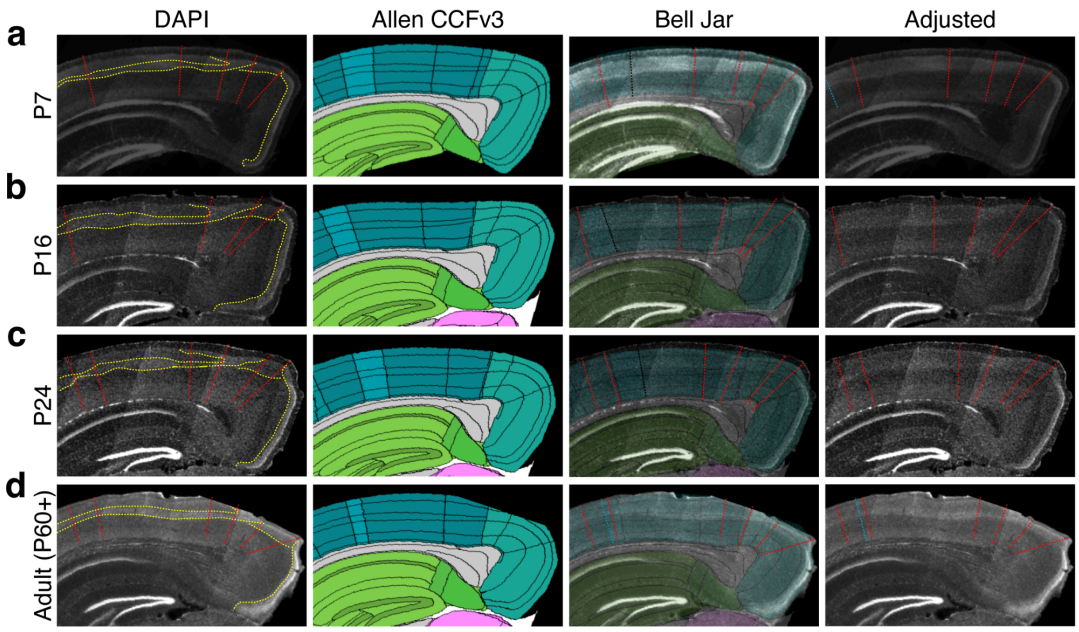

Figure 14. Cortical area alignment and registration across developmental and adult stages using Bell Jar and the Allen Brain CCFv3.

(a–d) Representative coronal sections from P7 **(a),** P16 **(b),** P24 **(c)**, and adult **(d)** brains showing DAPI-stained visual cortical areas (first column). Yellow dotted lines indicate layer 4 and other anatomical landmarks used to guide area boundary delineation, marked by red dotted lines. Corresponding Allen Brain CCFv3 reference images are shown in the second column. Bell Jar–aligned images are shown in the third column, with newly generated area boundaries (blue dotted lines) and boundaries excluded based on human evaluation (black dotted lines). Final adjusted boundaries (red and blue lines) reflecting manual refinement across developmental stages are shown in the fourth column.

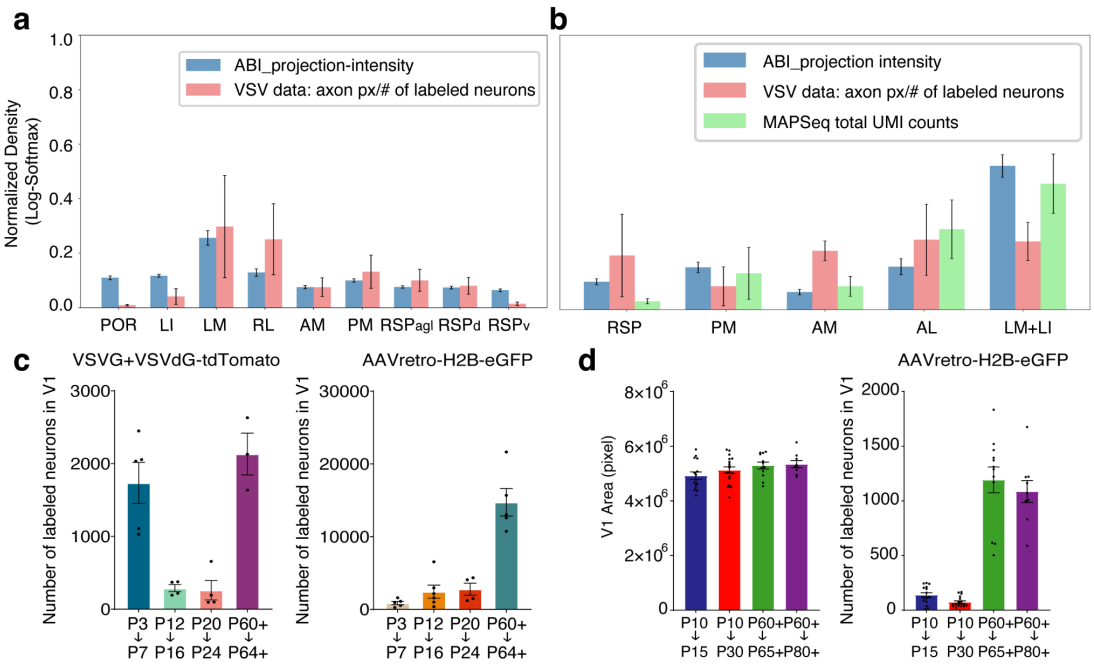

Figure 15. Adult V1 connectivity across tracing methods and developmental quantification of starter neurons.

(a) Comparison of adult V1 connectivity data from the Allen Brain Institute (ABI) atlas with VSVG+VSVdG-tdTomato quantification from the P60+→P64 group across multiple HVAs. **(b)** Comparison of three datasets across five micro-dissected areas used for MAPseq analysis: adult V1 connectivity from the ABI atlas, VSVG+VSVdG-tdTomato data from the P60+→P64 group, and total UMI counts from MAPseq in the P60+→P62 group**.** n=16 mice from ABI connectivity atlas, n= 3 for VSVG+VSVdG-tdTomato, n=7 for MAPseq datasets. Data are presented as mean ± SD. **(c)** Quantification of the number of starter neurons labeled in V1 for both VSVG+VSVdG-tdTomato and AAVretro-H2B-eGFP tracing experiments. For VSVG+VSVdG-tdTomato: n = 5 mice for P3→P7, n = 4 for P12→P16, n = 4 for P20→P24, and n = 3 for P60+→P64+. For AAVretro-H2B-eGFP: n = 5 mice for P3→P7, n = 6 for P12→P16, n = 4 for P20→P24, and n = 5 for P60+→P64+. Data are presented as mean ± SEM. **(d)** Quantification of V1 area size and the number of labeled V1 neurons per section from AAVretro-H2B-eGFP tracing experiments. Data were collected from 15 sections for P10→P15, 18 sections for P10→P30, 12 sections for P60+→P65+, and 9 sections for P60+→P80+, with 3 sections analyzed per animal.

Table 1. Animal and Experimental Condition Summary					
Cohort	Age_{end}	Mouse Strain	Sex	Procedure Conditions	ID
CTB	P6	C57BL6/J	?	CTB 555 5nL to AL, CTB 647 5nL to PM	M287
CTB	P6	C57BL6/J	?	CTB 647 10nL to PM, CTB 555 10nL to AL	M336
CTB	P6	C57BL6/J CHD8	?	CTB 647 10-15 nL to PM, CTB 555 10-15 nL to AL	JR0301
CTB	P6	C57BL6/J	?	CTB 647 10-15 nL to PM, CTB 555 10-15 nL to AL	JR0303
CTB	P9	C57BL6/J	?	CTB 647 10nL to AL, CTB 555 10nL to PM	M324
CTB	P9	C57BL6/J SepW1Cre	?	CTB 647 10nL to AL, CTB 555 10nL to PM	M349
CTB	P9	C57BL6/J dCas9-KRAB	?	CTB 647 20-25 nL to PM, CTB 555 20-25 nL to AL	JR0126
CTB	P9	C57BL6/J SepW1Cre	?	CTB 647 20-25 nL to PM, CTB 555 20-25 nL to AL	JR0131
CTB	P9	C57BL6/J	?	CTB 647 10-15 nL to PM, CTB	JR0158

		SepW1Cre		555 10-15 nL to AL	
CTB	P9	C57BL6/J Tlx3Cre	?	CTB 555 10-15 nL to PM, CTB 657 10-15 nL to AL	JR0143
CTB	P18	C57BL6/J VipFlp/CRC re	M	CTB 488 ~10nL to V1, CTB 555 ~10nL to AL, CTB 647 ~10nL to PM	K857
CTB	P18	C57BL6/J Nr5a1Cre	?	CTB 647 ~10nL to V1, CTB 488 ~10nL to AL, CTB 555 ~10nL to PM	K894
CTB	P18	C57BL6/J Nr5a1Cre	?	CTB 555 ~10nL to V1, CTB 647 ~10nL to AL, CTB 488 ~10nL to PM	K895
CTB	P65+	U	?	CTB 555 to PM, CTB 647 to AL, CTB 488 to LM	G19
CTB	P65+	U	?	CTB 555 to PM, CTB 647 to LM, CTB 488 to AL	G14
CTB	P65+	U	?	CTB 555 to PM, CTB 647 to LM, CTB 488 to AL	G03
AAVretro	P40	C57BL6/J SepW1Cre	?	P3: scAAVretro-hSyn-H2B-mCherry ~20 nL to PM P30: scAAVretro-hSyn-H2B-eGFP ~20 nL to AL	JR0103
AAVretro	P40	C57BL6/J SepW1Cre	?	P3: scAAVretro-hSyn-H2B-mCherr	JR0104

				y ~20 nL to PM P30: scAAVretro-hSyn-H2B-eGFP ~20 nL to AL	
AAVretro	P40	C57BL6/J dCas9-KRAB	?	P3: scAAVretro-hSyn-H2B-mCherry ~20 nL to PM P30: scAAVretro-hSyn-H2B-eGFP ~20 nL to AL	JR0105
AAVretro	P45	C57BL6/J SepW1Cre	?	P3: scAAVretro-hSyn-H2B-mCherry ~5-15 nL to PM P35: ~15-25 nL scAAVretro-hSyn-H2B-eGFP ~20 nL to AL	JR0356
AAVretro	P45	C57BL6/J SepW1Cre	?	P3: scAAVretro-hSyn-H2B-mCherry ~5-15 nL to PM P35: ~15-25 nL scAAVretro-hSyn-H2B-eGFP ~20 nL to AL	JR0357
AAVretro	P40	C57BL6/J Tlx3Cre	F	P30: scAAVretro-hSyn-H2B-mCherry ~20 nL to PM, scAAVRetro-hSyn-H2B-eGFP ~20 nL to AL	JR0755
AAVretro	P40	C57BL6/J Tlx3Cre	F	P30: scAAVretro-hSyn-H2B-mCherry ~20 nL to PM, scAAVRetro-hSyn-H2B-eGFP	JR0759

				~20 nL to AL	
AAVretro	P45	C57BL6/J SepW1Cre	F	P30: scAAVretro-hSyn-H2B-mCherry ~50 nL to PM, scAAVRetro-hSyn-H2B-eGFP ~50 nL to AL	JR0196
AAVretro	P45	C57BL6/J SepW1Cre	F	P30: scAAVretro-hSyn-H2B-mCherry ~50 nL to PM, scAAVRetro-hSyn-H2B-eGFP ~50 nL to AL	JR0197
AAVretro	P45	C57BL6/J SepW1Cre	F	P30: scAAVretro-hSyn-H2B-mCherry ~50 nL to PM, scAAVRetro-hSyn-H2B-eGFP ~50 nL to AL	JR0199
VSV + AAVretro	P7	C57BL6/J SepW1Cre	?	VSVG+VSVdG-tdTomato 5-10nL to V1	M487
VSV + AAVretro	P7	C57BL6/J SepW1Cre	?	VSVG+VSVdG-tdTomato 5-10nL to V1	M488
VSV + AAVretro	P7	C57BL6/J SepW1Cre	?	VSVG+VSVdG-tdTomato 5-10nL to V1	M496
VSV + AAVretro	P7	C57BL6/J Tlx3Cre	?	VSVG+VSVdG-tdTomato + scAAVretro-hSyn-H2B-eGFP [1:1] 50nL to V1	M729
VSV + AAVretro	P7	C57BL6/J Tlx3Cre	?	VSVG+VSVdG-tdTomato + scAAVretro-hSyn-H2B-eGFP [1:1] 50nL to V1	M730

VSV + AAVretro	P7	C57BL6/J SepW1Cre	?	AAV8-CAG-FLEX-tdTomato + scAAVretro-hSyn-H2B-eGFP [1:1] ~5-10nL to V1	M789/J R0249
VSV + AAVretro	P7	C57BL6/J SepW1Cre	?	AAV8-CAG-FLEX-tdTomato + scAAVretro-hSyn-H2B-eGFP [1:1] ~10-20nL to V1	M795/J R0276
VSV + AAVretro	P7	C57BL6/J SepW1Cre	?	AAV8-CAG-FLEX-tdTomato + scAAVretro-hSyn-H2B-eGFP [1:1] ~10-20nL to V1	M796
VSV + AAVretro	P16	C57BL6/J	?	VSVG+VSVdG-tdTomato + scAAVretro-hSyn-H2B-eGFP [1:1] ~5-10nL to V1	M677
VSV + AAVretro	P16	C57BL6/J	?	VSVG+VSVdG-tdTomato + scAAVretro-hSyn-H2B-eGFP [1:1] ~5-10nL to V1	M678
VSV + AAVretro	P16	C57BL6/J	?	VSVG+VSVdG-tdTomato + scAAVretro-hSyn-H2B-eGFP [1:1] ~50nL to V1	M704
VSV + AAVretro	P16	C57BL6/J	?	VSVG+VSVdG-tdTomato + scAAVretro-hSyn-H2B-eGFP [1:1] ~50nL to V1	M705
VSV + AAVretro	P16	C57BL6/J	?	VSVG+VSVdG-tdTomato + scAAVretro-hSyn-H2B-eGFP [1:1] ~50nL to V1	M711
VSV + AAVretro	P24	C57BL6/J	F	VSVG+VSVdG-tdTomato + scAAVretro-hSyn-H2B-eGFP [1:1] ~5-10nL to V1	M648

VSV + AAVretro	P24	C57BL6/J	F	VSVG+VSVdG-tdTomato + scAAVretro-hSyn-H2B-eGFP [1:1] ~5-10nL to V1	M649
VSV + AAVretro	P24	C57BL6/J	F	VSVG+VSVdG-tdTomato + scAAVretro-hSyn-H2B-eGFP [1:1] ~50nL to V1	M712
VSV + AAVretro	P24	C57BL6/J	F	VSVG+VSVdG-tdTomato + scAAVretro-hSyn-H2B-eGFP [1:1] ~50nL to V1	M715
VSV + AAVretro	P64+	C57BL6/J Tlx3Cre	F	VSVG+VSVdG-tdTomato + 1x PBS [1:1] ~100nL to V1	M608
VSV + AAVretro	P64+	C57BL6/J Tlx3Cre	F	VSVG+VSVdG-tdTomato + 1x PBS [1:1] ~100nL to V1	M609
VSV + AAVretro	P64+	C57BL6/J Tlx3Cre	F	VSVG+VSVdG-tdTomato + 1x PBS [1:1] ~100nL to V1	M610
VSV + AAVretro	P64+	C57BL6/J Tlx3Cre	M	AAV8-CAG-FLEX-tdTomato + scAAVretro-hSyn-H2B-eGFP [1:1] ~20-50nL to V1	M762? JR0038
VSV + AAVretro	P64+	C57BL6/J Tlx3Cre	F	AAV8-CAG-FLEX-tdTomato + scAAVretro-hSyn-H2B-eGFP [1:1] ~20-50nL to V1	M763/JR0039
VSV + AAVretro	P64+	C57BL6/J Tlx3Cre	F	AAV8-CAG-FLEX-tdTomato + scAAVretro-hSyn-H2B-eGFP [1:1] ~20-50nL to V1	M764/JR0040
VSV + AAVretro	P64+	C57BL6/J SepW1Cre	M	AAV8-CAG-FLEX-tdTomato + scAAVretro-hSyn-H2B-eGFP	M773/JR0166

				[1:1] 100nL to V1	
VSV + AAVretro	P64+	C57BL6/J SepW1Cre	F	AAV8-CAG-FLEX-tdTomato + scAAVretro-hSyn-H2B-eGFP [1:1] 50nL to V1	M776/J R0169
AAVretro	P15	C57BL6/J SepW1Cre	?	scAAVRetro-hSyn-H2B-eGFP ~10-20nL to LM	JR0567
AAVretro	P15	C57BL6/J Tlx3Cre	?	scAAVRetro-hSyn-H2B-eGFP ~10-20nL to LM	JR0534
AAVretro	P15	C57BL6/J	?	scAAVRetro-hSyn-H2B-eGFP ~10-20nL to LM	JR0537
AAVretro	P15	C57BL6/J Tlx3Cre	?	scAAVRetro-hSyn-H2B-eGFP ~10-20nL to LM	JR0612
AAVretro	P30	C57BL6/J Tlx3Cre	?	scAAVRetro-hSyn-H2B-eGFP ~10-20nL to LM	JR0531
AAVretro	P30	C57BL6/J Tlx3Cre	?	scAAVRetro-hSyn-H2B-eGFP ~10-20nL to LM	JR0564
AAVretro	P30	C57BL6/J Tlx3Cre	?	scAAVRetro-hSyn-H2B-eGFP ~10-20nL to LM	JR0532
AAVretro	P30	C57BL6/J Tlx3Cre	?	scAAVRetro-hSyn-H2B-eGFP ~10-20nL to LM	JR0561
AAVretro	P15	C57BL6/J Tlx3Cre	?	scAAVRetro-hSyn-H2B-eGFP ~10-20nL to LM	JR0533
AAVretro	P30	C57BL6/J	?	scAAVRetro-hSyn-H2B-eGFP	JR0560

		Tlx3Cre		~10-20nL to LM	
AAVretro	P15	C57BL6/J SepW1Cre	?	scAAVRetro-hSyn-H2B-eGFP ~10-20nL to LM	JR0741
AAVretro	P15	C57BL6/J Tlx3Cre	?	scAAVRetro-hSyn-H2B-eGFP ~10-20nL to LM	JR0744
AAVretro	P65+	C57BL6/J	M	scAAVRetro-hSyn-H2B-eGFP ~10-20nL to LM	JR0650
AAVretro	P65+	C57BL6/J Tlx3Cre	F	scAAVRetro-hSyn-H2B-eGFP ~10-20nL to LM	JR0684
AAVretro	P65+	C57BL6/J Tlx3Cre	F	scAAVRetro-hSyn-H2B-eGFP ~10-20nL to LM	JR0697
AAVretro	P65+	C57BL6/J Tlx3Cre	F	scAAVRetro-hSyn-H2B-eGFP ~10-20nL to LM	JR0698
AAVretro	P80+	C57BL6/J SepW1Cre	M	scAAVRetro-hSyn-H2B-eGFP ~10nL to LM	JR0659
AAVretro	P80+	C57BL6/J SepW1Cre	M	scAAVRetro-hSyn-H2B-eGFP ~10nL to LM	JR0662
AAVretro	P80+	C57BL6/J SepW1Cre	M	scAAVRetro-hSyn-H2B-eGFP ~10nL to LM	JR0663
MAPseq	P6.5	C57BL6/J	?	Sindbis Virus Library L2.2 mappnl-gfp 20nl to V1	M760
MAPseq	P6.5	C57BL6/J	?	Sindbis Virus Library L2.2 mappnl-gfp 20nl to V1	M761

MAPseq	P7	C57BL6/J	?	Sindbis Virus Library L2.2 mappnl-gfp ~15-25nL to V1	JR0375
MAPseq	P7	C57BL6/J	?	Sindbis Virus Library L2.2 mappnl-gfp ~15-25nL to V1	JR0376
MAPseq	P16	C57BL6/J	?	Sindbis Virus Library L2.2 mappnl-gfp ~50nL to V1	JR0422
MAPseq	P16	C57BL6/J	?	Sindbis Virus Library Vamp2 ~50nL to V1	JR0670
MAPseq	P16	C57BL6/J	?	Sindbis Virus Library Vamp2 ~50nL to V1	JR0671
MAPseq	P16	C57BL6/J	?	Sindbis Virus Library Vamp2 ~50-60nL to V1	JR0686
MAPseq	P24	C57BL6/J	M	Sindbis Virus Library Vamp2 ~50-60nL to V1	JR0672
MAPseq	P24	C57BL6/J	M	Sindbis Virus Library Vamp2 ~50-60nL to V1	JR0674
MAPseq	P24	C57BL6/J	F	Sindbis Virus Library Vamp2 ~50-60nL to V1	JR0678
MAPseq	P89	C57BL6/J	F	Sindbis Virus Library Vamp2 ~100nL to V1	JR0446
MAPseq	P78	C57BL6/J	F	Sindbis Virus Library L2.2 mappnl-gfp ~100nL to V1	JR0448

MAPseq	P84	C57BL6/J	M	Sindbis Virus Library L2.2 mappnl-gfp ~100nL to V1	JR0547
MAPseq	P84	C57BL6/J	M	Sindbis Virus Library L2.2 mappnl-gfp ~100nL to V1	JR0548
MAPseq	P75	C57BL6/J	F	Sindbis Virus Library L2.2 mappnl-gfp ~100nL to V1	JR0552
MAPseq	P76	C57BL6/J	M	Sindbis Virus Library Vamp2 ~100nL to V1	JR0692
MAPseq	P76	C57BL6/J	M	Sindbis Virus Library Vamp2 ~100nL to V1	JR0695
MAPseq	P75	C57BL6/J	M	Sindbis Virus Library Vamp2 ~100nL to V1	JR0694

Table 2. VSV-tdTomato ANOVA and Multiple Comparison Statistics

VSV-tdTomato	ANOVA Summary					Uncorrected Fisher's LSD		
Area	F	P value	P value summary	Significant diff. among means (P < 0.05)?	R squared	p3to7 vs. P12	P12 vs. P20	P12 vs. P60
RSPv	1.813	0.1985	ns	No	0.3118	ns (0.071)	ns (0.072)	ns (0.112)
RSPd	1.651	0.2301	ns	No	0.2921	ns (0.060)	ns (0.437)	ns (0.151)
RSPagl	1.809	0.1992	ns	No	0.3114	ns (0.122)	ns (0.712)	ns (0.321)
PM	2.504	0.1088	ns	No	0.385	ns (0.100)	ns (0.635)	ns (0.159)
AM	2.668	0.095	ns	No	0.4001	ns (0.058)	ns (0.830)	ns (0.145)
A	0.9239	0.4589	ns	No	0.1876	ns (0.483)	ns (0.980)	ns (0.359)
RL	8.115	0.0032	**	Yes	0.6698	*** (0.001)	** (0.004)	* (0.021)
AL	3.445	0.0517	ns	No	0.4627	* (0.011)	ns (0.156)	* (0.036)
LM	5.396	0.0139	*	Yes	0.5743	** (0.002)	ns (0.056)	* (0.024)
LI	5.681	0.0117	*	Yes	0.5868	** (0.003)	* (0.012)	** (0.009)
POR	2.096	0.1542	ns	No	0.3438	* (0.038)	ns (0.169)	ns (0.075)

Table 3. AAVretro-H2B-eGFP ANOVA and Multiple Comparison Statistics

AAVretro-H2B-eGFP	ANOVA Summary					Uncorrected Fisher's LSD		
Area	F	P value	P value summary	Significant diff. among means (P < 0.05)?	R squared	p3to7 vs. P12	P12 vs. P20	P12 vs. P60
RSPv	7.233	0.0028	**	Yes	0.5756	* (0.0445)	ns (0.1633)	ns (0.4689)
RSPd	6.182	0.0054	**	Yes	0.5368	* (0.0314)	ns (0.1531	ns (0.9962)
RSPagl	0.9903	0.4224	ns	No	0.1566	ns (0.6231)	ns (0.3885)	ns (0.9363)
PM	2.588	0.0891	ns	No	0.3267	* (0.0396)	* (0.0376)	ns (0.7622)
AM	1.173	0.351	ns	No	0.1803	ns (0.1365)	ns (0.1510)	ns (0.3631)
A	0.7468	0.5399	ns	No	0.1228	ns (0.6047)	ns (0.7924)	ns (0.5278)
RL	1.233	0.3304	ns	No	0.1877	ns (0.8941)	ns (0.9184)	ns (0.1682)
AL	0.7597	0.533	ns	No	0.1247	ns (0.8162)	ns (0.2879)	ns (0.1894)
LM	1.378	0.2854	ns	No	0.2053	ns (0.3043)	ns (0.2841)	ns (0.2346)
LI	0.4196	0.7414	ns	No	0.07293	ns (0.3576)	ns (0.8932)	ns (0.7476)
POR	0.3153	0.8141	ns	No	0.05581	ns (0.9794)	ns (0.4119)	ns (0.4458)

Table 4. Summary Statistics for Anterograde Tracing Method Similarity.

Summary statistics:

Data	Mean	Median	SD	Min	Max
ABI: n = 16	0.2749	0.2601	0.1150	0.0584	0.5492
VSV: n = 3	0.4697	0.5218	0.3139	0.3139	0.5736
MAPseq: n = 3	0.4228	0.4580	0.2018	0.2018	0.6083

Between-dataset mean JSD values:

ABI–VSV: 0.2553	ABI–MAPseq: 0.1510	VSV–MAPseq: 0.2597

Each of these values falls below the mean ABI–ABI JSD, suggesting cross-dataset similarity on par with internal ABI variation.

Kolmogorov–Smirnov (KS) p-values by area:

Comparison	LM+LI	AL	AM	PM	RSP
ABI vs. VSV	0.04128	0.3591	0.00206	0.8142	0.5046
ABI vs. MAPseq	0.2492	0.6504	0.2492	0.2054	0.00109
VSV vs. MAPseq	0.4000	0.8500	0.1667	0.9333	0.4000

Table 5. MAPseq Motif Distribution Statistics

Motifs	Age	Obs.	Exp.	Exp. SD	Effect Size	P-value
['RSP']	P12	13	32	5.5230	-1.2454	1.80E-04
['PM']	P12	63	32	5.5230	0.9473	6.83E-07
['AM']	P12	81	32	5.5230	1.3048	1.00E-10
['AL']	P12	20	32	5.5230	-0.6604	2.35E-02
['LM']	P12	241	32	5.5230	2.8661	1.00E-10
['RSP', 'PM']	P12	6	8	2.8182	-0.3702	5.94E-01
['RSP', 'AM']	P12	4	8	2.8182	-0.8556	2.09E-01
['RSP', 'AL']	P12	2	8	2.8182	-1.5926	3.02E-02
['RSP', 'LM']	P12	5	8	2.8182	-0.5926	3.73E-01
['PM', 'AM']	P12	45	8	2.8182	2.3460	1.00E-10
['PM', 'AL']	P12	2	8	2.8182	-1.5926	3.02E-02
['PM', 'LM']	P12	24	8	2.8182	1.4663	3.35E-06
['AM', 'AL']	P12	3	8	2.8182	-1.1776	7.47E-02
['AM', 'LM']	P12	39	8	2.8182	2.1444	1.00E-10
['AL', 'LM']	P12	27	8	2.8182	1.6298	8.72E-08
['RSP', 'PM', 'AM']	P12	4	2	1.4161	0.7312	1.45E-01
['RSP', 'PM', 'AL']	P12	0	2	1.4161	-1.5907	2.78E-01
['RSP', 'PM', 'LM']	P12	4	2	1.4161	0.7312	1.45E-01
['RSP', 'AM', 'AL']	P12	0	2	1.4161	-1.5907	2.78E-01
['RSP', 'AM', 'LM']	P12	0	2	1.4161	-1.5907	2.78E-01
['RSP', 'AL', 'LM']	P12	1	2	1.4161	-0.5907	7.29E-01
['PM', 'AM', 'AL']	P12	1	2	1.4161	-0.5907	7.29E-01
['PM', 'AM', 'LM']	P12	14	2	1.4161	2.3162	2.82E-08
['PM', 'AL', 'LM']	P12	2	2	1.4161	-0.0057	1.00E+00
['AM', 'AL', 'LM']	P12	6	2	1.4161	1.2167	1.68E-02
['RSP', 'PM', 'AM', 'AL']	P12	0	0	0.7089	-0.5878	1.00E+00
['RSP', 'PM', 'AM', 'LM']	P12	5	0	0.7089	1.9971	1.75E-04
['RSP', 'PM', 'AL', 'LM']	P12	0	0	0.7089	-0.5878	1.00E+00
['RSP', 'AM', 'AL', 'LM']	P12	0	0	0.7089	-0.5878	1.00E+00

['PM', 'AM', 'AL', 'LM']	P12	1	0	0.7089	0.4122	3.95E-01
['RSP', 'PM', 'AM', 'AL', 'LM']	P12	1	0	0.3546	0.8291	1.18E-01
['RSP']	P20	7	25	4.9439	-1.7439	1.69E-05
['PM']	P20	20	25	4.9439	-0.3516	2.67E-01
['AM']	P20	148	25	4.9439	2.4753	1.00E-10
['AL']	P20	122	25	4.9439	2.1986	1.00E-10
['LM']	P20	103	25	4.9439	1.9565	1.00E-10
['RSP', 'PM']	P20	0	6	2.5227	-2.8970	2.50E-03
['RSP', 'AM']	P20	9	6	2.5227	0.4249	3.15E-01
['RSP', 'AL']	P20	1	6	2.5227	-1.8970	2.59E-02
['RSP', 'LM']	P20	4	6	2.5227	-0.5751	4.29E-01
['PM', 'AM']	P20	5	6	2.5227	-0.3120	8.41E-01
['PM', 'AL']	P20	0	6	2.5227	-2.8970	2.50E-03
['PM', 'LM']	P20	1	6	2.5227	-1.8970	2.59E-02
['AM', 'AL']	P20	13	6	2.5227	0.9104	1.60E-02
['AM', 'LM']	P20	12	6	2.5227	0.8034	4.27E-02
['AL', 'LM']	P20	37	6	2.5227	2.3509	1.00E-10
['RSP', 'PM', 'AM']	P20	3	1	1.2676	0.6147	2.20E-01
['RSP', 'PM', 'AL']	P20	1	1	1.2676	-0.3853	1.00E+00
['RSP', 'PM', 'LM']	P20	0	1	1.2676	-1.3853	4.19E-01
['RSP', 'AM', 'AL']	P20	0	1	1.2676	-1.3853	4.19E-01
['RSP', 'AM', 'LM']	P20	0	1	1.2676	-1.3853	4.19E-01
['RSP', 'AL', 'LM']	P20	1	1	1.2676	-0.3853	1.00E+00
['PM', 'AM', 'AL']	P20	1	1	1.2676	-0.3853	1.00E+00
['PM', 'AM', 'LM']	P20	1	1	1.2676	-0.3853	1.00E+00
['PM', 'AL', 'LM']	P20	1	1	1.2676	-0.3853	1.00E+00
['AM', 'AL', 'LM']	P20	2	1	1.2676	0.1997	6.78E-01
['RSP', 'PM', 'AM', 'AL']	P20	0	0	0.6346	-0.4886	1.00E+00
['RSP', 'PM', 'AM', 'LM']	P20	0	0	0.6346	-0.4886	1.00E+00
['RSP', 'PM', 'AL', 'LM']	P20	0	0	0.6346	-0.4886	1.00E+00
['RSP', 'AM', 'AL', 'LM']	P20	0	0	0.6346	-0.4886	1.00E+00

['PM', 'AM', 'AL', 'LM']	P20	0	0	0.6346	-0.4886	1.00E+00
['RSP', 'PM', 'AM', 'AL', 'LM']	P20	0	0	0.3174	-0.1385	1.00E+00
['RSP']	P60+	25	110	10.2554	-2.1068	1.00E-10
['PM']	P60+	160	110	10.2554	0.5237	6.75E-06
['AM']	P60+	75	110	10.2554	-0.5593	2.50E-04
['AL']	P60+	470	110	10.2554	2.0723	1.00E-10
['LM']	P60+	886	110	10.2554	2.9855	1.00E-10
['RSP', 'PM']	P60+	33	27	5.2330	0.2421	2.93E-01
['RSP', 'AM']	P60+	9	27	5.2330	-1.5235	7.43E-05
['RSP', 'AL']	P60+	5	27	5.2330	-2.2604	2.62E-07
['RSP', 'LM']	P60+	29	27	5.2330	0.0615	7.74E-01
['PM', 'AM']	P60+	29	27	5.2330	0.0615	7.74E-01
['PM', 'AL']	P60+	10	27	5.2330	-1.3860	1.74E-04
['PM', 'LM']	P60+	84	27	5.2330	1.5640	1.00E-10
['AM', 'AL']	P60+	9	27	5.2330	-1.5235	7.43E-05
['AM', 'LM']	P60+	21	27	5.2330	-0.3860	2.15E-01
['AL', 'LM']	P60+	177	27	5.2330	2.6303	1.00E-10
['RSP', 'PM', 'AM']	P60+	5	6	2.6295	-0.4036	7.00E-01
['RSP', 'PM', 'AL']	P60+	3	6	2.6295	-0.9886	1.79E-01
['RSP', 'PM', 'LM']	P60+	26	6	2.6295	1.7663	2.20E-08
['RSP', 'AM', 'AL']	P60+	1	6	2.6295	-1.9886	1.95E-02
['RSP', 'AM', 'LM']	P60+	0	6	2.6295	-2.9886	1.81E-03
['RSP', 'AL', 'LM']	P60+	5	6	2.6295	-0.4036	7.00E-01
['PM', 'AM', 'AL']	P60+	3	6	2.6295	-0.9886	1.79E-01
['PM', 'AM', 'LM']	P60+	20	6	2.6295	1.4037	3.78E-05
['PM', 'AL', 'LM']	P60+	12	6	2.6295	0.7118	8.12E-02
['AM', 'AL', 'LM']	P60+	7	6	2.6295	0.0114	8.50E-01
['RSP', 'PM', 'AM', 'AL']	P60+	0	1	1.3164	-1.4511	4.28E-01
['RSP', 'PM', 'AM', 'LM']	P60+	3	1	1.3164	0.5489	2.52E-01
['RSP', 'PM', 'AL', 'LM']	P60+	5	1	1.3164	1.1338	3.18E-02
['RSP', 'AM', 'AL', 'LM']	P60+	0	1	1.3164	-1.4511	4.28E-01

['PM', 'AM', 'AL', 'LM']	P60+	5	1	1.3164	1.1338	3.18E-02
['RSP', 'PM', 'AM', 'AL', 'LM']	P60+	0	0	0.6584	-0.5196	1.00E+00

Table 6. MAPseq Motif Effect Trajectory Statistics.

Motif	Transition	P-value	Significant
RSP	P3 to P12	1.38E-01	ns
RSP	P12 to P20	4.98E-01	ns
RSP	P20 to P60	6.50E-01	ns
PM	P3 to P12	1.21E-04	***
PM	P12 to P20	8.13E-05	****
PM	P20 to P60	5.45E-03	**
AM	P3 to P12	3.89E-01	ns
AM	P12 to P20	6.80E-12	****
AM	P20 to P60	3.38E-61	****
AL	P3 to P12	1.24E-15	****
AL	P12 to P20	1.39E-27	****
AL	P20 to P60	2.32E-01	ns
LM	P3 to P12	6.97E-05	****
LM	P12 to P20	5.03E-11	****
LM	P20 to P60	8.29E-19	****
PM+RSP	P3 to P12	5.53E-01	ns
PM+RSP	P12 to P20	3.66E-02	*
PM+RSP	P20 to P60	1.36E-03	**
AM+RSP	P3 to P12	7.39E-01	ns
AM+RSP	P12 to P20	9.23E-02	ns
AM+RSP	P20 to P60	2.70E-03	**
AL+RSP	P3 to P12	5.62E-01	ns
AL+RSP	P12 to P20	1.00E+00	ns
AL+RSP	P20 to P60	1.00E+00	ns
LM+RSP	P3 to P12	7.76E-01	ns
LM+RSP	P12 to P20	1.00E+00	ns

LM+RSP	P20 to P60	5.00E-01	ns
AM+PM	P3 to P12	1.58E-14	****
AM+PM	P12 to P20	1.06E-07	****
AM+PM	P20 to P60	6.62E-01	ns
AL+PM	P3 to P12	7.18E-01	ns
AL+PM	P12 to P20	5.06E-01	ns
AL+PM	P20 to P60	2.24E-01	ns
LM+PM	P3 to P12	2.41E-01	ns
LM+PM	P12 to P20	1.36E-05	****
LM+PM	P20 to P60	6.17E-07	****
AL+AM	P3 to P12	3.77E-03	**
AL+AM	P12 to P20	3.92E-03	**
AL+AM	P20 to P60	3.09E-05	****
AM+LM	P3 to P12	1.89E-06	****
AM+LM	P12 to P20	2.19E-03	**
AM+LM	P20 to P60	2.18E-02	*
AL+LM	P3 to P12	1.26E-01	ns
AL+LM	P12 to P20	3.74E-02	*
AL+LM	P20 to P60	5.85E-01	ns
AM+PM+RSP	P3 to P12	2.16E-02	*
AM+PM+RSP	P12 to P20	1.00E+00	ns
AM+PM+RSP	P20 to P60	1.78E-01	ns
AL+PM+RSP	P3 to P12	1.00E+00	ns
AL+PM+RSP	P12 to P20	4.45E-01	ns
AL+PM+RSP	P20 to P60	5.67E-01	ns
LM+PM+RSP	P3 to P12	1.00E+00	ns
LM+PM+RSP	P12 to P20	1.33E-01	ns
LM+PM+RSP	P20 to P60	9.02E-03	**

AL+AM+RSP	P3 to P12	5.27E-01	ns
AL+AM+RSP	P12 to P20	1.00E+00	ns
AL+AM+RSP	P20 to P60	1.00E+00	ns
AM+LM+RSP	P3 to P12	1.00E+00	ns
AM+LM+RSP	P12 to P20	1.00E+00	ns
AM+LM+RSP	P20 to P60	1.00E+00	ns
AL+LM+RSP	P3 to P12	1.00E+00	ns
AL+LM+RSP	P12 to P20	1.00E+00	ns
AL+LM+RSP	P20 to P60	1.00E+00	ns
AL+AM+PM	P3 to P12	4.16E-01	ns
AL+AM+PM	P12 to P20	1.00E+00	ns
AL+AM+PM	P20 to P60	5.67E-01	ns
AM+LM+PM	P3 to P12	8.93E-04	***
AM+LM+PM	P12 to P20	2.71E-03	**
AM+LM+PM	P20 to P60	1.56E-01	ns
AL+LM+PM	P3 to P12	4.96E-01	ns
AL+LM+PM	P12 to P20	1.00E+00	ns
AL+LM+PM	P20 to P60	4.83E-01	ns
AL+AM+LM	P3 to P12	1.00E+00	ns
AL+AM+LM	P12 to P20	3.11E-01	ns
AL+AM+LM	P20 to P60	6.81E-01	ns
AL+AM+PM+RSP	P3 to P12	1.00E+00	ns
AL+AM+PM+RSP	P12 to P20	1.00E+00	ns
AL+AM+PM+RSP	P20 to P60	1.00E+00	ns
AM+LM+PM+RSP	P3 to P12	3.37E-02	*
AM+LM+PM+RSP	P12 to P20	6.96E-02	ns
AM+LM+PM+RSP	P20 to P60	1.00E+00	ns
AL+LM+PM+RSP	P3 to P12	5.27E-01	ns

AL+LM+PM+RSP	P12 to P20	1.00E+00	ns
AL+LM+PM+RSP	P20 to P60	5.91E-01	ns
AL+AM+LM+RSP	P3 to P12	1.00E+00	ns
AL+AM+LM+RSP	P12 to P20	1.00E+00	ns
AL+AM+LM+RSP	P20 to P60	1.00E+00	ns
AL+AM+LM+PM	P3 to P12	1.64E-01	ns
AL+AM+LM+PM	P12 to P20	1.00E+00	ns
AL+AM+LM+PM	P20 to P60	5.91E-01	ns
AL+AM+LM+PM+RSP	P3 to P12	1.00E+00	ns
AL+AM+LM+PM+RSP	P12 to P20	1.00E+00	ns
AL+AM+LM+PM+RSP	P20 to P60	1.00E+00	ns

Glossary of Abbreviations

AAV	Adeno-associated virus
AAVretro	Retrograde-capable adeno-associated virus
AL	Anterolateral visual area (HVA)
AM	Anteromedial visual area (HVA)
ANOVA	Analysis of variance
CCFv3	Common Coordinate Framework version 3 (Allen Institute)
CCPN	Cortico-cortical projection neuron
CTB	Cholera toxin subunit B
DAPI	4′,6-diamidino-2-phenylindole
DL	Deep-layer (cluster type)
GC	Genome copies
H2B	Histone H2B (nuclear localization tag)
HVA	Higher visual area

IACUC	Institutional Animal Care and Use Committee
LI	Laterointermediate visual area (HVA)
LM	Lateromedial visual area (HVA)
LP	Lateral posterior nucleus (Thalamic area)
MAPseq	Multiplexed Analysis of Projections by Sequencing
ML	Multi-layer (cluster type)
NA	Numerical aperture (microscopy)
NP	Non-projecting (cluster type)
PBS	Phosphate-buffered saline
PFA	Paraformaldehyde
PM	Posteromedial visual area (HVA)
POR	Postrhinal cortex (HVA)
PVA-DABCO	Polyvinyl alcohol with DABCO (antifade mounting medium)
RSAT	Recursive Signal Averaging and Thresholding

RSP	Retrosplenial cortex (HVA)
RSPagl	Agranular retrosplenial cortex (CCFv3 HVA)
RSPd	Dorsal retrosplenial cortex (CCFv3 HVA)
RSPv	Ventral retrosplenial cortex (CCFv3 HVA)
SEM	Standard error of the mean
UMI	Unique molecular identifier
V1	Primary visual cortex
VISal	Visual area anterolateral (CCFv3 HVA) (see also, AL)
VISam	Visual area anteromedial (CCFv3 HVA) (see also, AM)
VISl	Visual area lateromedial (CCFv3 HVA) (see also, LM)
VISli	Visual area laterointermediate (CCFv3 HVA) (see also, LI)
VISpm	Visual area posteromedial (CCFv3 HVA) (see also, PM)
VISpor	Visual area postrhinal (CCFv3 HVA) (see also, POR)
VISrl	Visual area rostrolateral (CCFv3 HVA) (see also, RL)

VSV	Vesicular stomatitis virus
VSVG	Vesicular stomatitis virus glycoprotein
VSVdG	Glycoprotein-deleted vesicular stomatitis virus
dLGN	Dorsal lateral geniculate nucleus (Thalamic area)
eGFP	Enhanced green fluorescent protein
tdTomato	Tandem dimer Tomato (a red fluorescent protein)

References

Baker, J.T., Holmes, A.J., Masters, G.A., Yeo, B.T.T., Krienen, F., Buckner, R.L., and Öngür, D. (2014). Disruption of cortical association networks in schizophrenia and psychotic bipolar disorder. JAMA Psychiatry *71*, 109–118. https://doi.org/10.1001/jamapsychiatry.2013.3469.

Barone, P., Dehay, C., Berland, M., and Kennedy, H. (1996). Role of directed growth and target selection in the formation of cortical pathways: prenatal development of the projection of area V2 to area V4 in the monkey. J. Comp. Neurol. *374*, 1–20. https://doi.org/10.1002/(SICI)1096-9861(19961007)374:1<1::AID-CNE1>3.0.CO;2-7.

Bridle, J. (1989). Training stochastic model recognition algorithms as networks can lead to maximum mutual information estimation of parameters. Neural Inf Process Syst, 211–217.

Cai, L., Argunşah, A.Ö., Damilou, A., and Karayannis, T. (2024). A nasal chemosensation-dependent critical window for somatosensory development. Science *384*, 652–660. https://doi.org/10.1126/science.adn5611.

Calinski, T., and Harabasz, J. (1974). A dendrite method for cluster analysis. Commun. Stat. Theory Methods *3*, 1–27. https://doi.org/10.1080/03610927408827101.

Callaway, E.M., and Katz, L.C. (1990). Emergence and refinement of clustered horizontal connections in cat striate cortex. J. Neurosci. *10*, 1134–1153. https://doi.org/10.1523/JNEUROSCI.10-04-01134.1990.

Cheng, S., Butrus, S., Tan, L., Xu, R., Sagireddy, S., Trachtenberg, J.T., Shekhar, K., and Zipursky, S.L. (2022). Vision-dependent specification of cell types and function in the developing cortex. Cell *185*, 311–327.e24. https://doi.org/10.1016/j.cell.2021.12.022.

Chen, X., Fischer, S., Rue, M.C.P., Zhang, A., Mukherjee, D., Kanold, P.O., Gillis, J., and Zador, A.M. (2024). Whole-cortex in situ sequencing reveals input-dependent area identity. Nature. https://doi.org/10.1038/s41586-024-07221-6.

Davies, D.L., and Bouldin, D.W. (1979). A Cluster Separation Measure. IEEE Trans. Pattern Anal. Mach. Intell. *PAMI-1*, 224–227. https://doi.org/10.1109/tpami.1979.4766909.

Felleman, D.J., and Van Essen, D.C. (1991). Distributed hierarchical processing in the primate cerebral cortex. Cereb. Cortex *1*, 1–47. https://doi.org/10.1093/cercor/1.1.1-a.

Garrett, M.E., Nauhaus, I., Marshel, J.H., and Callaway, E.M. (2014). Topography and areal organization of mouse visual cortex. J. Neurosci. *34*, 12587–12600. https://doi.org/10.1523/JNEUROSCI.1124-14.2014.

Glickfeld, L.L., Andermann, M.L., Bonin, V., and Reid, R.C. (2013). Cortico-cortical projections in mouse visual cortex are functionally target specific. Nat. Neurosci. *16*, 219–226. https://doi.org/10.1038/nn.3300.

Haberl, M.G., Zerbi, V., Veltien, A., Ginger, M., Heerschap, A., and Frick, A. (2015). Structural-functional connectivity deficits of neocortical circuits in the Fmr1 (-/y) mouse model of autism. Sci. Adv. *1*, e1500775. https://doi.org/10.1126/sciadv.1500775.

Hackett, T. A. (2011). Information flow in the auditory cortical network. Hearing Research, 271(1–2), 133–146. https://doi.org/10.1016/j.heares.2010.01.011

Han, X., and Bonin, V. (2024). Higher-order cortical and thalamic pathways shape visual processing streams in the mouse cortex. Curr. Biol. https://doi.org/10.1016/j.cub.2024.10.048.

Han, Y., Kebschull, J.M., Campbell, R.A.A., Cowan, D., Imhof, F., Zador, A.M., and Mrsic-Flogel, T.D. (2018). The logic of single-cell projections from visual cortex. Nature *556*, 51–56. https://doi.org/10.1038/nature26159.

Hand, R.A., Khalid, S., Tam, E., and Kolodkin, A.L. (2015). Axon Dynamics during Neocortical Laminar Innervation. Cell Rep. *12*, 172–182. https://doi.org/10.1016/j.celrep.2015.06.026.

Harris, J.A., Mihalas, S., Hirokawa, K.E., Whitesell, J.D., Choi, H., Bernard, A., Bohn, P., Caldejon, S., Casal, L., Cho, A., et al. (2019). Hierarchical organization of cortical and thalamic connectivity. Nature *575*, 195–202. https://doi.org/10.1038/s41586-019-1716-z.

Harris, K. D. & Mrsic-Flogel, T. D. (2013) .Cortical connectivity and sensory coding. Nature 503, 51–58. https://doi.org/10.1038/nature12654.

Innocenti, G.M., Fiore, L., and Caminiti, R. (1977). Exuberant projection into the corpus callosum from the visual cortex of newborn cats. Neurosci. Lett. *4*, 237–242. https://doi.org/10.1016/0304-3940(77)90185-9.

Innocenti, G.M., and Price, D.J. (2005). Exuberance in the development of cortical

networks. Nat. Rev. Neurosci. *6*, 955–965. https://doi.org/10.1038/nrn1790.

Kast, R.J., and Levitt, P. (2019). Precision in the development of neocortical architecture: From progenitors to cortical networks. Prog. Neurobiol. *175*, 77–95. https://doi.org/10.1016/j.pneurobio.2019.01.003.

Katz, L.C., and Shatz, C.J. (1996). Synaptic activity and the construction of cortical circuits. Science *274*, 1133–1138. https://doi.org/10.1126/science.274.5290.1133.

Kebschull, J.M., Garcia da Silva, P., Reid, A.P., Peikon, I.D., Albeanu, D.F., and Zador, A.M. (2016). High-throughput mapping of single-neuron projections by sequencing of barcoded RNA. Neuron *91*, 975–987. https://doi.org/10.1016/j.neuron.2016.07.036.

Kim, E.J., Zhang, Z., Huang, L., Ito-Cole, T., Jacobs, M.W., Juavinett, A.L., Senturk, G., Hu, M., Ku, M., Ecker, J.R., et al. (2020). Extraction of Distinct Neuronal Cell Types from within a Genetically Continuous Population. Neuron *107*, 274–282.e6. https://doi.org/10.1016/j.neuron.2020.04.018.

Klingler, E., Tomasello, U., Prados, J., Kebschull, J.M., Contestabile, A., Galiñanes, G.L., Fièvre, S., Santinha, A., Platt, R., Huber, D., et al. (2021). Temporal controls over inter-areal cortical projection neuron fate diversity. Nature *599*, 453–457. https://doi.org/10.1038/s41586-021-04048-3.

Kronman, F.N., Liwang, J.K., Betty, R., Vanselow, D.J., Wu, Y.-T., Tustison, N.J., Bhandiwad, A., Manjila, S.B., Minteer, J.A., Shin, D., et al. (2024). Developmental mouse brain common coordinate framework. Nat. Commun. *15*, 9072. https://doi.org/10.1038/s41467-024-53254-w.

Liwang, J.K., Kronman, F.A., Minteer, J.A., Wu, Y.-T., Vanselow, D.J., Ben-Simon, Y., Taormina, M., Parmaksiz, D., Way, S.W., Zeng, H., et al. (2023). epDevAtlas: Mapping GABAergic cells and microglia in postnatal mouse brains. bioRxivorg. https://doi.org/10.1101/2023.11.24.568585.

Li, Z., Li, P., Pan, H., Adams, A.M.J., Huang, Z., Liu, H., Li, J., Su, Y., Zhong, B., Bray, L., et al. (2025). D-LMBmapX: Generalized deep-learning pipeline for automated whole-brain neural circuitry profiling across any developmental stages. bioRxiv. https://doi.org/10.1101/2025.02.25.639766.

Luo, L., and O'Leary, D.D.M. (2005). Axon retraction and degeneration in development and disease. Annu. Rev. Neurosci. *28*, 127–156. https://doi.org/10.1146/annurev.neuro.28.061604.135632.

MacQueen, J. B. Some Methods for Classification and Analysis of MultiVariate

Observations. in Proc. of the fifth Berkeley Symposium on Mathematical Statistics and Probability (eds. Cam, L. M. L. & Neyman, J.) 1, 281–297 (University of California Press, 1967).

Majtey, A.P., Lamberti, P.W., and Prato, D.P. (2005). Jensen-Shannon divergence as a measure of distinguishability between mixed quantum states. Phys. Rev. A *72*, 052310. https://doi.org/10.1103/PhysRevA.72.052310.

Markov, N.T., Vezoli, J., Chameau, P., Falchier, A., Quilodran, R., Huissoud, C., Lamy, C., Misery, P., Giroud, P., Ullman, S., et al. (2014). Anatomy of hierarchy: feedforward and feedback pathways in macaque visual cortex. J. Comp. Neurol. *522*, 225–259. https://doi.org/10.1002/cne.23458.

Marshel, J.H., Garrett, M.E., Nauhaus, I., and Callaway, E.M. (2011). Functional specialization of seven mouse visual cortical areas. Neuron *72*, 1040–1054. https://doi.org/10.1016/j.neuron.2011.12.004.

Molyneaux, B.J., Arlotta, P., Menezes, J.R.L., and Macklis, J.D. (2007). Neuronal subtype specification in the cerebral cortex. Nat. Rev. Neurosci. *8*, 427–437. https://doi.org/10.1038/nrn2151.

Murakami, T., Matsui, T., and Ohki, K. (2017). Functional segregation and development of mouse higher visual areas. J. Neurosci. *37*, 9424–9437. https://doi.org/10.1523/JNEUROSCI.0731-17.2017.

Murakami, T., Matsui, T., Uemura, M., and Ohki, K. (2022). Modular strategy for development of the hierarchical visual network in mice. Nature *608*, 578–585. https://doi.org/10.1038/s41586-022-05045-w.

Oh, S.W., Harris, J.A., Ng, L., Winslow, B., Cain, N., Mihalas, S., Wang, Q., Lau, C., Kuan, L., Henry, A.M., et al. (2014). A mesoscale connectome of the mouse brain. Nature *508*, 207–214. https://doi.org/10.1038/nature13186.

Robinson, S., Poorman, C.E., Marder, T.J., and Bucci, D.J. (2012). Identification of functional circuitry between retrosplenial and postrhinal cortices during fear conditioning. J. Neurosci. *32*, 12076–12086. https://doi.org/10.1523/JNEUROSCI.2814-12.2012.

Rousseeuw, P.J. (1987). Silhouettes: A graphical aid to the interpretation and validation of cluster analysis. J. Comput. Appl. Math. *20*, 53–65. https://doi.org/10.1016/0377-0427(87)90125-7.

Sanes, J.R., and Lichtman, J.W. (1999). Development of the vertebrate neuromuscular junction. Annu. Rev. Neurosci. *22*, 389–442. https://doi.org/10.1146/annurev.neuro.22.1.389.

Siu, C., Balsor, J., Merlin, S., Federer, F., and Angelucci, A. (2021). A direct interareal feedback-to-feedforward circuit in primate visual cortex. Nat. Commun. *12*, 4911. https://doi.org/10.1038/s41467-021-24928-6.

Smith, I.T., Townsend, L.B., Huh, R., Zhu, H., and Smith, S.L. (2017). Stream-dependent development of higher visual cortical areas. Nat. Neurosci. *20*, 200–208. https://doi.org/10.1038/nn.4469.

Soronow, A.L.R., Jacobs, M.W., Dickson, R.G., and Kim, E.J. (2025). Bell Jar: A semiautomated registration and cell counting tool for mouse neurohistology analysis. eNeuro *12*. https://doi.org/10.1523/ENEURO.0036-23.2025.

Wang, Q., and Burkhalter, A. (2007). Area map of mouse visual cortex. J. Comp. Neurol. *502*, 339–357. https://doi.org/10.1002/cne.21286.

Wang, Q., Ding, S.-L., Li, Y., Royall, J., Feng, D., Lesnar, P., Graddis, N., Naeemi, M., Facer, B., Ho, A., et al. (2020). The Allen Mouse Brain Common Coordinate Framework: A 3D reference atlas. Cell *181*, 936–953.e20. https://doi.org/10.1016/j.cell.2020.04.007.

Ward, J.H., Jr (1963). Hierarchical grouping to optimize an objective function. J. Am. Stat. Assoc. *58*, 236–244. https://doi.org/10.1080/01621459.1963.10500845.

Watakabe, A., and Hirokawa, J. (2018). Cortical networks of the mouse brain elaborate within the gray matter. Brain Struct. Funct. *223*, 3633–3652. https://doi.org/10.1007/s00429-018-1710-5.

Watakabe, A., Skibbe, H., Nakae, K., Abe, H., Ichinohe, N., Rachmadi, M.F., Wang, J., Takaji, M., Mizukami, H., Woodward, A., et al. (2023). Local and long-distance organization of prefrontal cortex circuits in the marmoset brain. Neuron *0*. https://doi.org/10.1016/j.neuron.2023.04.028.

Yasuda, M., Nagappan-Chettiar, S., Johnson-Venkatesh, E.M., and Umemori, H. (2021). An activity-dependent determinant of synapse elimination in the mammalian brain. Neuron *109*, 1333–1349.e6. https://doi.org/10.1016/j.neuron.2021.03.006.

Young, H., Belbut, B., Baeta, M., and Petreanu, L. (2021). Laminar-specific cortico-cortical loops in mouse visual cortex. Elife *10*. https://doi.org/10.7554/eLife.59551.

Zeki, S., and Shipp, S. (1988). The functional logic of cortical connections. Nature *335*, 311–317. https://doi.org/10.1038/335311a0.